



MMP-Responsive Nanomaterials

Journal:	<i>Biomaterials Science</i>
Manuscript ID	BM-REV-05-2023-000840.R1
Article Type:	Review Article
Date Submitted by the Author:	18-Jul-2023
Complete List of Authors:	<p>Son, Jiye; CUNY Advanced Science Research Center, Nanoscience Initiative</p> <p>Parveen, Sadiyah; CUNY Advanced Science Research Center, Nanoscience Initiative; CUNY City College, Department of Biomedical Engineering</p> <p>MacPherson, Douglas; CUNY Advanced Science Research Center, Nanoscience Initiative; CUNY Graduate Center, Ph.D. Program in Biochemistry; Memorial Sloan Kettering Cancer Center, Department of Radiology; Hunter College CUNY, Department of Chemistry</p> <p>Marciano, Yaron; CUNY Advanced Science Research Center, Nanoscience Initiative; CUNY Graduate Center, Ph.D. Program in Chemistry; CUNY Brooklyn College, Department of Chemistry</p> <p>Huang, Richard; CUNY Advanced Science Research Center, Nanoscience Initiative</p> <p>Ulijn, Rein ; CUNY Advanced Science Research Center, Nanoscience Initiative; CUNY Graduate Center, Ph.D. Program in Biochemistry; CUNY Graduate Center, Ph.D. Program in Chemistry; Hunter College CUNY, Department of Chemistry</p>

REVIEW

MMP-Responsive Nanomaterials

Jiye Son, ^{†a} Sadiyah Parveen, ^{†a,b} Douglas MacPherson, ^{a,c,e,f} Yaron Marciano, ^{a,f} Richard H. Huang, ^a and Rein V. Ulijn ^{*a,c,d,g}Received 00th January 20xx,
Accepted 00th January 20xx

DOI: 10.1039/x0xx00000x

Matrix metalloproteinases (MMP) are enzymes that degrade the extracellular matrix and regulate essential normal cell behaviors. Inhibition of these enzymes has been a strategy for anti-cancer therapy since 1990s, but with limited success. A new type of MMP-targeting strategy exploits the innate selective hydrolytic activity and consequent catalytic signal amplification of the proteinases, rather than inhibiting it. Using nanomaterials, the enzymatic chemical reaction can trigger the temporal and spatial activation of the anti-cancer effects, amplify the associated response, and cause mechanical damage or report on cancer cells. We analyzed nearly 60 literature studies that incorporate chemical design strategies that lead to spatial, temporal, and mechanical control of the anti-cancer effect through four modes of action: nanomaterial shrinkage, induced aggregation, formation of cytotoxic nanofibers, and activation by de-PEGylation. From the literature analysis, we derived chemical design guidelines to control and enhance MMP activation of nanomaterials of various chemical compositions (peptide, lipid, polymer, inorganic). Finally, the review includes a guide on how multiple characteristics of the nanomaterial, such as substrate modification, supramolecular structure, and electrostatic charge should be collectively considered for the targeted MMP to result in optimal kinetics of enzyme action on the nanomaterial, which allow access to amplification and additional levels of spatial, temporal, and mechanical control of the response. Although this review focuses on the design strategies of MMP-responsive nanomaterials in cancer applications, these guidelines are expected to be generalizable to systems that target MMP for treatment or detection of cancer and other diseases, as well as other enzyme-responsive nanomaterials.

1. Introduction

Matrix metalloproteinases (MMP) are a family of enzymes that are responsible for degrading components of the extracellular matrix and for regulating extracellular cell signals that are essential to normal cell behaviors such as turnover of tissues, angiogenesis, and wound healing. Atypical activation and overexpression of MMPs have been linked to multiple diseases including arthritis,¹ cardiovascular diseases,² multiple types of cancers,^{3–8} and their progression.⁹ MMP-responsive materials have been developed for several biomedical applications, including targeted delivery of small and biomolecular therapeutic agents, imaging, phototherapy, as well as sensors to detect and quantify MMP levels *in vitro* and *in vivo*. Direct methods of inhibiting the MMP catalytic activity include using small molecule inhibitors,¹⁰ or using collagen peptidomimetics which typically contain a collagen-like backbone to facilitate binding to the active site of the MMP and a hydroxamate structure which inactivates the enzyme through chelating the zinc ion (Zn²⁺) in the active site.^{11,12} Indirect methods include blocking MMP gene expression, or interfering with MMP's interactions with other proteins.^{13,14} However, while they often show promising *in vitro* performance, these strategies have proven to be largely unsuccessful in clinical trials and MMPs remain as highly desirable, yet unattained targets.¹⁵

The interest in targeting MMPs for anti-cancer treatment is evident from the number of projects undertaken by the pharmaceutical industry. Since the late 1990s, more than 50

^a Nanoscience Initiative, Advanced Science Research Center at The Graduate Center of the City University of New York (CUNY), 85 Saint Nicholas Terrace, New York, NY 10031, USA. Email: rulijn@gc.cuny.edu

^b Department of Biomedical Engineering, The City College of New York, CUNY, 160 Convent Avenue, New York, NY 10031, USA.

^c Ph.D. Program in Biochemistry, The Graduate Center of CUNY, 365 Fifth Avenue, New York, NY 10016, USA.

^d Ph.D. Program in Chemistry, The Graduate Center of CUNY, 365 Fifth Avenue, New York, NY 10016, USA.

^e Department of Radiology, Memorial Sloan Kettering Cancer Center, 1275 York Avenue, New York, New York 10065, USA.

^f Department of Chemistry, Brooklyn College, CUNY, 2900 Bedford Avenue, Brooklyn, NY 11210, USA.

^g Department of Chemistry, Hunter College, CUNY, 695 Park Avenue, New York, NY 10065, USA.

[†] These authors are considered as co-first authors.

MMP-responsive anti-cancer systems have been tested in clinical trials and these systems continue to show potential for targeted anti-cancer therapy.¹⁶ Although many broad spectrum MMP inhibitors¹⁷ demonstrated promising preclinical data, and were evaluated in clinical trials, these trials were cancelled in phase III due to a lack of efficacy or severe toxicity.^{16,18} The failures in clinical trials have allowed researchers to discover new roles of MMPs in various stages and grades of different cancers, leading to a more comprehensive understanding of the functions of MMPs through technological developments.¹⁶ Major reasons for the limited success include non-specific inhibition of the different MMPs (23 human MMPs) -which have similar substrate pockets- and the timing of the MMP inhibition during cancer progression, which leads to broad inhibition of MMPs, including those that have anti-cancer effects at specific stages of cancer.^{16,19} Despite the challenges, researchers continue to investigate ways to target MMPs using inhibitors²⁰ and to develop new and innovative strategies for targeting MMPs in cancer.

1.1. MMP-targeting nanomaterials for anti-cancer therapy

Within the past ~ 20 years, a new type of MMP-targeting strategy has been explored which exploits the innate selective hydrolytic activity of the proteinases -rather than inhibiting it- to trigger anti-cancer effects using nanomaterials. This strategy could be advantageous because it is autonomous, whereby the desired anti-cancer effect can be expected to be triggered in areas where MMP activity is upregulated during specific stages of cancer progression. There are a number of unique advantages to this strategy compared to the approach of inhibiting MMP activity. First, the catalytic trigger inherently **amplifies** a signal through the process of catalytic turnover (Fig. 1A). This means that each MMP molecule can turnover large numbers of nanostructured substrates, which leads to signal amplification in the material response compared to the 1:1 stoichiometry in small molecule inhibition. Second, the approach can be used to convert and amplify disease-specific signals to supramolecular changes, providing access to **physical** or **mechanical** action such as a micelle to fiber morphology switch (Fig. 1B). Lastly, using MMP-responsive materials, an ideal system could selectively engage with a specific MMP target, activate at the site where it is needed (i.e., the tumor microenvironment rather than a healthy environment), and respond at a pre-defined rate (ranging from a few hours to multiple days) giving rise to **spatial** and **temporal** controlled therapeutic or diagnostic effect (Fig. 1C).

This manuscript reviews the promising results of these strategies by categorizing the examples found in literature into 4 different modes of action: 1) nanomaterial shrinkage or collapse, 2) induced aggregation, 3) formation of cytotoxic amyloid-like fibers, and 4) activation by de-PEGylation. We evaluate how the 4 different modes of response affect the efficacy of the therapeutic or imaging agent *in vitro* and *in vivo*. Typically, the design of MMP-responsive nanomaterial is simplified to inserting an MMP-cleavable peptide sequence into a known material. For our analysis, we applied a more holistic

approach using three additional factors: 1) sequence specificity, 2) supramolecular architecture (with an emphasis on order/disorder) and 3) electrostatic recruitment and analyze examples in literature to derive general trends on how these factors can influence MMP specificity and affect the rate of nanomaterial response. Lastly, we discuss key challenges and opportunities for MMP-responsive nanomaterials to be translated into clinical use. Before diving into the specific examples of MMP-responsive nanomaterials, we provide the readers with context on MMP structure and function and their atypical activities during cancer progression.

1.2. Structures and properties of MMPs

MMPs are a family of zinc-dependent endopeptidases that remodel the extracellular matrix and are involved in extracellular cell signaling. Regulation of MMP activity and expression at the transcription and translational levels are necessary and crucial for maintaining normal biological processes.²¹ There are a total of 23 known MMPs found in humans which are either secreted from the cells or are bound to the cell surface membrane.²² Traditionally, MMPs were named after their common substrates, for example, MMP-1, -8, and -13 are also called collagenase 1, 2, and 3, respectively, and MMP-2 and -9 are called gelatinase A and B, respectively. As the names suggest, MMPs have different roles in tissue remodeling, which requires them to have specific interactions with their substrates. Following the discovery of many more substrates, they are now grouped together according to their domain structures and are sequentially numbered in the order of discovery.

All MMPs are initially expressed as inactive pro-enzymes or zymogens and are subsequently activated extracellularly (with the exception MMP-11 and -28)²³ when required through a "cysteine switch" process which breaks the Cys-Zn²⁺ interaction between the cysteine in the pro-enzyme domain and the Zn²⁺ in the catalytic domain of the enzyme. Three histidines in the catalytic domain's sequence, HEXXHXXGXXH, ligate the active site Zn²⁺ and the glutamate residue activates a zinc-bound H₂O molecule, providing the nucleophile responsible for cleaving the peptide bonds.²⁴ Once activated, MMP activity is regulated by a class of proteins called tissue inhibitors of metalloproteinases (TIMPs) which comprise of 4 homologous members (TIMP-1, -2, -3 and -4). TIMP-1, -2, and -4 are secreted proteins, whereas TIMP-3 is membrane bound and therefore restricted to the extracellular matrix.²⁵ TIMPs bind MMPs in a stoichiometric 1:1 ratio and can prevent substrates from accessing the catalytic domain of MMPs and inhibit MMP activity.²⁵ Detailed descriptions of the structures and functions of MMPs have been published by Nagase *et al.*^{21,22} Table 1 summarizes the 23 human MMPs with their cellular location, domain structure class, numerical and other names, natural substrates, and the pro and active form of the MMPs' calculated isoelectric points, molecular weights, and amino acid lengths. In section 3 of the review, we discuss how these inherent characteristics of MMP such as their isoelectric points are relevant in designing

electrostatically charged nanomaterials to match the enzyme's charge.

1.3. Role of MMPs and overexpression in cancer progression

The roles of MMPs in cancer progression have been studied since the 1980's and have been mainly associated with one of the hallmarks of cancer: tissue invasion and metastasis.²⁶ Since then, many other cancer development processes have been associated with MMPs, including cancer cell invasion, proliferation, apoptosis, tumor angiogenesis and vasculogenesis, cell adhesion, migration, and epithelial-mesenchymal transition, as well as escaping immune surveillance.^{9,13} The regulation of MMPs is a complex biological

process, and both down- or up- regulation of MMPs have been observed based on subtypes⁷ and stages⁸ of cancer. Of the different MMPs, MMP-2, -7, and -9 have been most widely studied for their overexpression during cancer progression.⁶ For example, in comparison to healthy volunteers, patients with colorectal cancer have concentrations that are ~43 times higher for MMP-2 and ~74 times higher for MMP-9 in colorectal tissues; and ~7.5 times higher for MMP-2 and ~3 times higher for MMP-9 in plasma.⁴ Table 2 lists nanomolar concentrations of MMP-2 and -9 measured in various cancer cell lines, mouse models, and patient-derived samples quantified using ELISA; and millimolar concentrations of MMP-7 reported by Tanaka *et al.*²⁷ from cell culture media of various cancer cell lines measured through fluorometric assays.

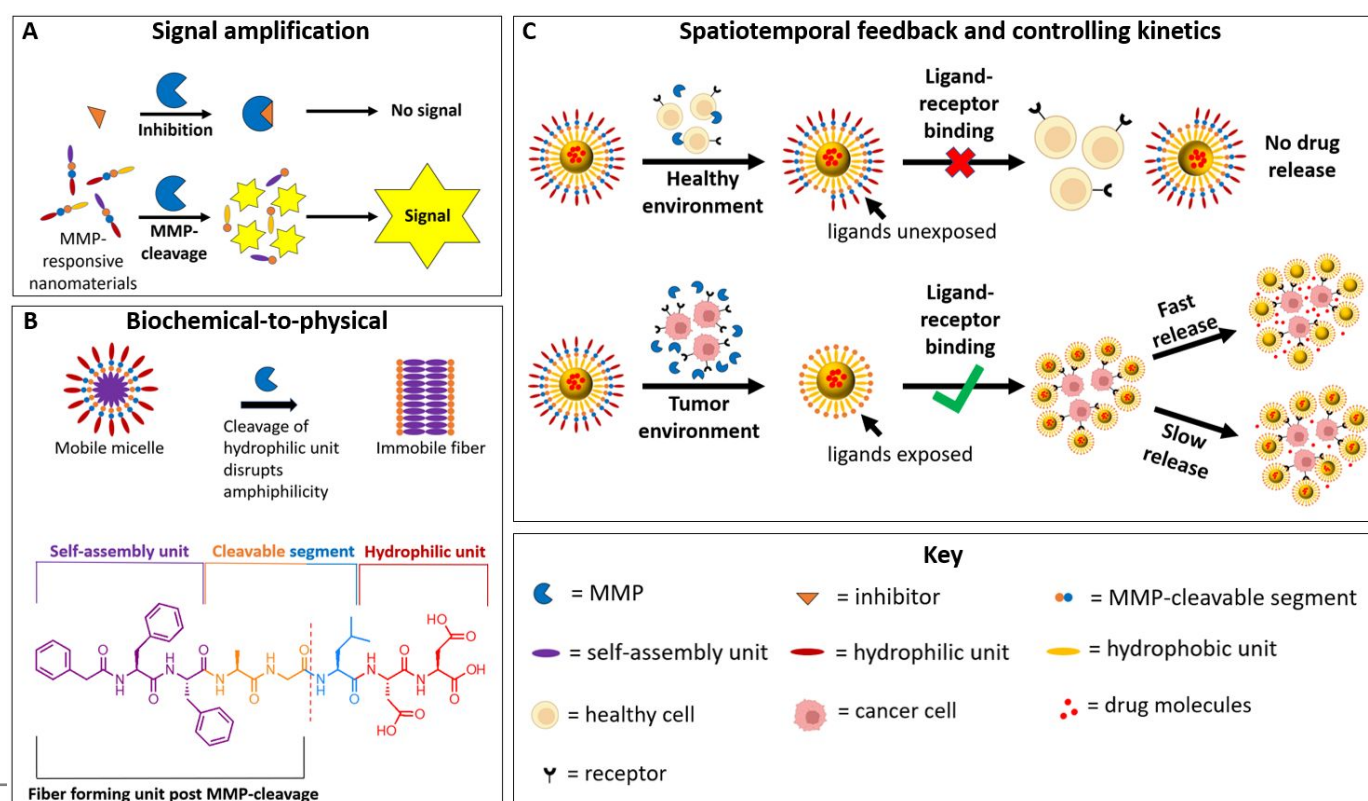


Fig. 1 MMP-responsive nanomaterials have the ability to (A) amplify the signal, (B) induce a physical morphology switch, and (C) control the spatial and temporal activation of the nanomaterial.

Table 1. Table of 23 human MMPs and their cellular location, domain structure class, numerical and other names, natural substrates, and characteristics. Adapted from references 13, 21, and 28 (N/A = not available).

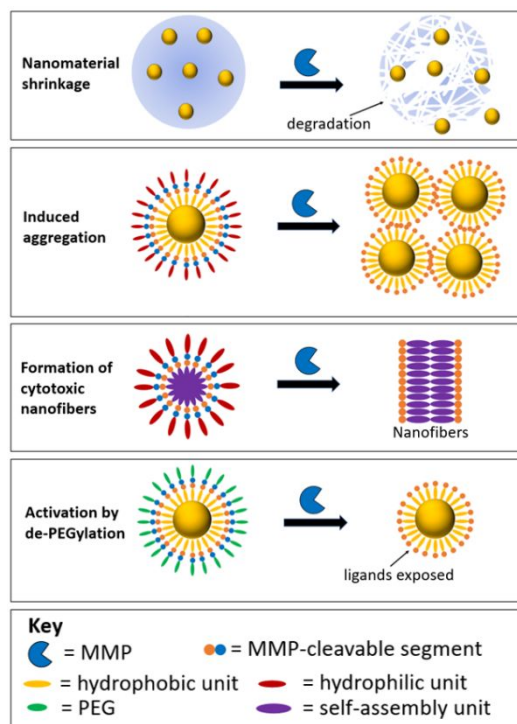
Domain Structure Class	MMPs	Other Name(s)	Natural Substrates	pI Pro	pI Active	MW (kDa) Pro	MW (kDa) Active	Length (amino acids) Pro	Length (amino acids) Active
Secreted									
Minimal domain	7	Matrilysin; matrin; PUMP1; small uterine metalloproteinase	Fibronectin; IGFBP-3; BM-40 (SPARC/Osteonectin); Decorin; E-cadherin; Fas ligand; Pro-TNF α ; RANK ligand; Heparin-binding EGF	7.73	8.77	28	19	267	173
	26	Matrilysin 2; endometase	N/A	5.96	N/A	28	19	261	N/A
Simple hemopexin domain	1	Collagenase 1; interstitial/fibroblast/tissue collagenase	Type I collagen; Fibronectin; IGFBP-3; IL-1 β degradation; Monocyte chemoattractant protein-3; Protease activated receptor 1	6.47	4.85	55	45	469	169
	3	Stromelysin 1; transin 1; proteoglycanase; procollagenase activating protein	Fibronectin; Basement membrane; E-cadherin; Plasminogen; Perlecan; IGFBP-3; BM-40 (SPARC/Osteonectin); Monocyte chemoattractant protein-3; Decorin	5.77	4.89	57	45	477	173
	8	Collagenase 2; neutrophil/PMN/granulocyte collagenase	Type I collagen	6.38	4.64	75	58	467	171
	10	Stromelysin 2; transin-2	N/A	5.49	4.68	57	44	476	173
	12	Metalloelastase; macrophage elastase/metalloelastase	Plasminogen	8.75	N/A	54	45,22	470	N/A
	13	Collagenase 3	Type I collagen; Perlecan; Monocyte chemoattractant protein-3	5.32	5.17	60	48	471	171
	19	RASI-1; MMP-18	IGFBP-3; Laminin 5 γ 2 chain	7.22	8.81	54	45	508	161
	20	Enamelysin	N/A	8.84	6.40	54	22	483	169
Gelatin-binding	27	N/A	N/A	8.83	N/A	N/A	N/A	513	N/A
	2	Gelatinase A; 72-kDa/neutrophil gelatinase; 72-kDa type IV collagenase	Chondroitin sulfate proteoglycan; Fibronectin; IGFBP-3; BM-40 (SPARC/Osteonectin); Laminin 5 γ 2 chain; IL-1 β degradation; Monocyte chemoattractant protein-3; Decorin; Big endothelin; Adrenomedullin; Stromal cell-derived factor 1 α	5.26	4.72	72	66	660	343
	9	Gelatinase B; 92-kDa gelatinase; 92-kDa type IV collagenase	BM-40 (SPARC/Osteonectin); ICAM-1; IL-1 β degradation; IL-2R α ; Precursor of TGF β ; Collagen IV; Galactin-3	5.69	4.88	92	86	707	343
	11	Stromelysin-3	N/A	6.38	5.19	51	44	488	169
Furin-activated and secreted	28	Epilysin	N/A	9.70	N/A	56	45	520	N/A
	21	Homologue of Xenopus XMMP	N/A	9.19	N/A	62	49	569	N/A
Membrane associated									
Trans-membrane	14	MT1-MMP; MT-MMP1	CD44; Type I collagen; Laminin 5 γ 2 chain; Monocyte chemoattractant protein-3; Cell surface tissue transglutaminase; Transmembrane mucin 1	7.63	4.89	66	56	582	187
	15	MT2-MMP; MT-MMP2	Cell surface tissue transglutaminase	7.03	N/A	72	50	669	N/A
	16	MT3-MMP; MT-MMP3	Cell surface tissue transglutaminase	8.72	N/A	64	52	607	N/A
	24	MT5-MMP; MT-MMP5	N/A	9.30	5.56	57	53	645	194
GPI-anchored	17	MT4-MMP; MT-MMP4	N/A	6.08	N/A	57	53	603	N/A
	25	MT6-MMP; MT-MMP6; leukolysin	N/A	8.76	N/A	34	28	562	N/A
Type II trans-membrane	23	Cysteine array MMP (CA-MMP); femalysin; MIFR	N/A	9.94	N/A	28	19	390	N/A

Table 2. Concentrations of MMP-2 and -9 in non-cancerous and 10 varieties of cancerous samples measured through ELISA assay; and concentrations of MMP -7 in cell culture media measured by fluorometric assay.

Cancer	Sample type	MMP	Concentration (ng/mL)	Assay	Ref.
Non-Cancerous	Healthy volunteer plasma	MMP-2	75 ± 5.7	ELISA	4
		MMP-9	20 ± 2.5	ELISA	
	Healthy volunteer colonic tissue	MMP-2	4.2 ± 0.4 (ng/mg)	ELISA	
		MMP-9	6.5 ± 3.5 (ng/mg)	ELISA	
Lung Cancer	Healthy volunteer plasma	MMP-9	36 ± 13	ELISA	29
		NSCLC patient plasma	MMP-9	71 ± 60	ELISA
	NSCLC mouse model - Heart	MMP-2	~0.3	ELISA	30
		MMP-2	~2 (ng/mg)	ELISA	
		MMP-2	~14 (ng/mg)	ELISA	
		MMP-2	~1 (ng/mg)	ELISA	
		MMP-2	~2 (ng/mg)	ELISA	
		MMP-2	~4 (ng/mg)	ELISA	
		MMP-2	~9 (ng/mg)	ELISA	
		MMP-2	~9 (ng/mg)	ELISA	
Breast cancer	4T1 cell culture media at 6 h	MMP-2	~1	ELISA	31
		MMP-2	~2	ELISA	
		MMP-2	~3	ELISA	
		MMP-2	~4	ELISA	
Prostate cancer	DU-145 cell culture media	MMP-2	0.46 ± 0.14	ELISA	32
		MMP-2	0.46 ± 0.14	ELISA	
Bladder carcinoma	RT-112 mice model tumor extract	MMP-2	1.5 ± 1.1	ELISA	33
		MMP-9	0.1 ± 0.01	ELISA	
Colorectal cancer	Patient plasma	MMP-2	570 ± 45	ELISA	4
		MMP-9	57 ± 7.9	ELISA	
	Patient colorectal tissue	MMP-2	180 ± 99 (ng/mg)	ELISA	
		MMP-9	480 ± 74 (ng/mg)	ELISA	
Pancreatic Cancer	MIAPaCa-2 cell culture media	MMP-9	0.008 ± 0.004	ELISA	34
		MMP-9	0.13 ± 0.023	ELISA	
Fibrosarcoma	HT1080 mice model tumor extract	MMP-2	17 ± 6.3	ELISA	33
		MMP-9	5.2 ± 1.7	ELISA	
	HT1080 cell culture media at 6 h	MMP-2	~30	ELISA	31
		MMP-2	~45	ELISA	
		MMP-2	~60	ELISA	
		MMP-2	~63	ELISA	
Glioblastoma	U-87 mice model tumor extract	MMP-2	16 ± 12	ELISA	33
		MMP-9	5.0 ± 1.0	ELISA	
Cancer	Sample type	MMP	Concentration (mg/mL)	Assay	Ref.
Non-Cancerous	Primary human pancreatic epithelial cell culture media	MMP-7	0.079 ± 0.025	Fluorometric	27
		MMP-7	0.32 ± 0.066	Fluorometric	
Breast Cancer	SKBR3 cell culture media	MMP-7	2.1 ± 0.92	Fluorometric	
		MMP-7	1.8 ± 1.3	Fluorometric	
Cervical Cancer	HeLa cell culture media	MMP-7	2.0 ± 0.66	Fluorometric	
Pancreatic Cancer	MIAPaCa-2 cell culture media	MMP-7	1.6 ± 0.84	Fluorometric	
Skin carcinoma	A431 cell culture media	MMP-7	1.3 ± 0.51	Fluorometric	

2. Four Modes of MMP-triggered responses for targeted anti-cancer therapy

Rather than inhibiting the action of MMPs, MMP-responsive nanomaterials are designed to take advantage of the inherent overexpression and activity of MMPs to trigger a nanomaterial response, allowing spatial and temporal control and amplification of the anti-cancer response. In Tables 3-6, MMP-responsive anti-cancer nanomaterials from literature are categorized into 4 different modes of responses following MMP action: 1) nanomaterial shrinkage, where the initial larger nanomaterials degrade to release encapsulated smaller nanoparticles or the larger structure breaks up into smaller parts; 2) nanomaterial aggregation where the change in surface charge or amphiphilicity results in an aggregated morphology with irregular forms that lack a clear structural pattern; 3) nanofiber formation where the switch of morphology from micelles into highly organized one-dimensional structures (such as amyloid-like fibers) influence cell behavior; and 4) de-PEGylation of the nanomaterial which exposes bioactive ligands that were previously shielded by the PEG layer and activates the anti-cancer effects (Fig. 2). As we review the different categories, we discuss how the different modes of response can influence the bioactivities *in vitro* and/or *in vivo*. Among these bioactivities are increased internalization and selective accumulation in tumors and cancer cells which enhances the efficacy of the therapeutic or imaging agent while reducing off-target effects.



2.1. Nanomaterial shrinkage

Nanomaterials that are 100-200 nm in size can have enhanced accumulation in the tumor microenvironment, but this accumulation is generally limited to the periphery of the tumor.³⁵ It has been proposed that by using nanomaterials that

Fig. 2 The MMP-triggered modes of response for anti-cancer therapy. As a response to MMP hydrolysis of the substrate in the nanomaterial, the nanomaterial can 1) shrink in size, 2) aggregate in size, 3) switch into cytotoxic nanofibers, or 4) reveal a functional moiety in the nanomaterial without changing in size.

reduce in size following cleavage by MMPs, the shrunken 10-40 nm particles have enhanced penetration into the interstitial tumor space. Wong *et al.* have used this strategy and decorated the surface of gelatin nanoparticles with quantum dots to form <100 nm nanoparticles (Fig. 3A).³⁶ After incubating the particles with MMP-2, 90% of the quantum dots (10 nm) were released from the gelatin particles over 12 h. When the MMP-responsive gelatin nanoparticles and non-responsive control silica particles embedded with quantum dots were directly injected into tumors *in vivo*, the quantum dots released from the gelatin particle had diffused 300 μm from the injection site, whereas the quantum dots on the silica particle remained localized in the initial injection location. This example demonstrated a proof-of-concept for MMP-triggered release of quantum dots allowing deeper penetration into the solid tumor mass. This strategy may also be applicable for other therapeutic molecules.

In another system, Nazli *et al.* developed magnetic iron oxide particles coated with an MMP-cleavable acrylate-PEG polymer loaded with doxorubicin (DOX).³⁷ These 229 nm particles shrunk to 59 nm after 1 day of incubation with bacteria-produced collagenase type I. Interestingly, this size shrinkage did not trigger an increase in DOX release until 3 days later. By day 4, 60% of DOX was released from the particles that were incubated with collagenase, in comparison to the 36% released without collagenase. We speculate that, although the nanoparticle's size was responsive to the enzymatic cleavage of the polymer coating, the rate of payload release is not simultaneously triggered by cleavage of the enzyme substrate. It is likely that the drugs remain embedded in the polymer coating which continues to degrade in solution over time. *In vitro*, the DOX-loaded MMP-responsive nanoparticles were internalized by HeLa cells 11 times more than non-responsive or bare iron oxide particles. In addition, the drug-loaded nanoparticles displayed time-dependent activity in which they were less cytotoxic to HeLa cells compared to free DOX at 24 and 48 h, but more cytotoxic at 72 h of incubation, corresponding with the release rate of DOX from the nanoparticle. This example demonstrated both the temporal and spatial control of the anti-cancer effects.

He *et al.* designed a "ball-and-rod" drug carrier system in which mesoporous silica nanoparticles and star polyethylene glycol (PEG) were connected *via* MMP-responsive peptide linkers (Fig. 3B).³⁸ When incubated with MMP-2 for 3 h, the size of the particles significantly decreased from ~ 100 nm to ~ 42 nm. *In vitro* studies on a multicellular 3D tumor spheroid showed that the fluorescence intensity of the particles decreased at a scanning depth of 40 μm because of the restricted penetration by the particles' large size. However, after 3 h of MMP-2 incubation, the tumor penetration increased significantly, demonstrating that MMP-2 could effectively decrease the particles' size and permit greater tumor penetration. *In vivo* imaging system (IVIS) revealed that, after injection of various Cy5.5-labeled carriers in mice, the accumulation of MMP-responsive particles in collected tumors was much higher than that of non-responsive control particles. Moreover, mice treated with DOX-loaded MMP-responsive particles displayed average tumor weights and volumes that were significantly

smaller than that of the non-responsive particles and free DOX. Furthermore, the tumor inhibition rate was significantly higher for the DOX-loaded MMP-responsive particles, compared to the non-responsive particles. This study demonstrated that due to MMP-2 activity, the resulting smaller particles could display an enhanced antitumor effect both *in vitro* and *in vivo*.

The above three examples as well as those outlined in Table 3 demonstrate that MMP-triggered shrunken nanoparticles can have enhanced internalization by cells *in vitro* and enhanced penetration in solid tumors *in vivo* allowing for spatial control of the anti-cancer effects. Compared to non-responsive structures, the responsive nanoparticles display enhanced

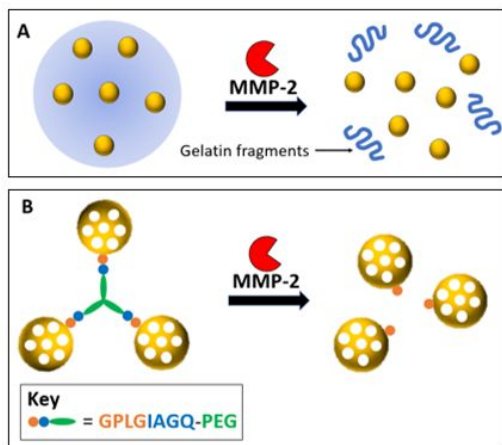


Fig. 3 Cartoon representation of (A) MMP-2-responsive size shrinking gelatin nanoparticles reproduced from reference 36 with permission from Copyright 2011 National Academy of Sciences, and (B) MMP-2-responsive mesoporous silica nanoparticles reproduced from reference 38 with permission from Copyright 2020 Royal Society of Chemistry.

imaging and therapeutic effects against cancer cells.

2.2. Induced aggregation

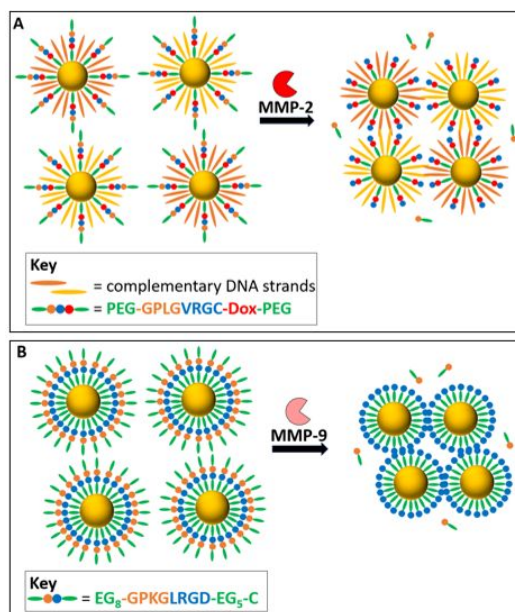
Nanomaterials can display increased accumulation and access in the tumor site owing to their reduced size as discussed in the previous section. In different contexts, an increase in particle size can also be advantageous. The examples listed in Table 4 demonstrate how designed material aggregation can effectively increase the penetration and retention of the material in the tumor site or cause cellular uptake by different endocytic pathways.

Using this strategy, Callmann *et al.* developed paclitaxel conjugated block-co-polymers using MMP-cleavable peptides as linkers to form 20 nm spherical particles. These particles enter the periphery of the tumor and aggregate upon MMP activation, keeping the material immobilized around the tumor tissue.³⁹ The aggregation of the polymer was observed in 4 h as a result of amphiphilic imbalance of the polymer building blocks after the substrate was cleaved by MMP-12. When evaluated *in vivo*, the tumor growth inhibition observed with the MMP-responsive paclitaxel conjugated nanomaterial was comparable to that of free paclitaxel, but with much lower systematic toxicity at a higher maximum tolerated dose.⁵⁰ The results

demonstrate that the induced aggregation strategy using MMP-cleavable polymeric nanocarriers allowed targeted transportation of chemotherapy drug molecules to the disease site while limiting off-target toxicity.

The MMP-triggered aggregation strategy can also be achieved by using inorganic nanoparticles. Yang *et al.* reported gold nanoparticles (AuNPs) grafted with complementary DNA strands, tethered with DOX, and encapsulated with PEG *via* a thermal-labile linker and an MMP-cleavable peptide (Fig. 4A).⁴⁰ Upon MMP-2 incubation, the protective PEG surface was removed and an increase in NP size from 73 nm to 1.8×10^6 nm was observed as a result of DNA hybridization. Compared to the MMP-inert controls, the MMP-responsive AuNPs showed significantly enhanced efficiency in photoacoustic (PA) imaging and photothermal conversion upon near-infrared irradiation. At 24 h post injection, the MMP-responsive AuNPs portrayed a 1.61-fold higher tumor uptake at each time point, compared to the non-responsive AuNPs. Additionally, *in vivo* studies on SCC-7 tumor-bearing mice revealed that the average tumor PA intensity of the mice treated with MMP-responsive AuNPs was 1.74-fold stronger compared to the mice treated with the control. Moreover, the tumor growth was almost completely inhibited in the mice treated with MMP-responsive AuNPs, compared to only a slight delay in tumor growth observed for the control groups. This study highlighted the potential of using MMP-induced AuNP aggregation as the source of strong near-infrared signal for deep-tissue imaging and chemo-photothermal therapy.

In a recent paper, our group also utilized the MMP-triggered aggregation strategy using AuNPs decorated with zwitterionic, self-complementary peptides. Similar to the previously mentioned hybridizing DNA strands, the peptides were used to drive the multivalent electrostatic interaction and aggregation of the NPs.⁴¹ In this system, AuNPs were grafted with an MMP-9 cleavable peptide ligand which exposed a self-complementary peptide sequence upon enzymatic action and induced aggregation of AuNPs (Fig. 4B). In MMP-9 overexpressing cancer cells, these aggregates formed in proximity of the cell membranes and gave rise to size-induced cellular uptake. Cancer cells treated with the MMP-responsive AuNPs showed significantly reduced viability (~50%), while the healthy cells were unaffected (~100%). The AuNP aggregates were visualized within cancer cells and were co-localized with endosomes and/or lysosomes, while no AuNP aggregates could be detected in healthy cells. Interestingly, a subtle change in the peptide sequence from GPKG↓LRGD to GPKL↓GRGD completely turned-off the MMP-responsiveness in the latter and caused cellular uptake by a different endocytic pathway which led to ~80% cell viability in cancer cells. This study demonstrated a potentially generalizable system for targeted drug-free cancer therapy *via* physical damage or interruption of cellular pathway through MMP-induced AuNP aggregation.

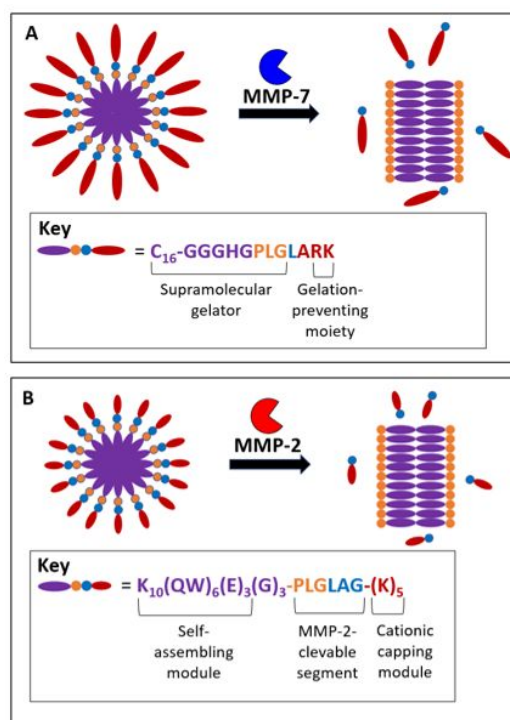


2.3. Formation of cytotoxic amyloid-like nanofibers

Enzymatically triggered formation of cytotoxic nanofibers is an emerging field in anti-cancer therapy. This mode of response was pioneered and extensively researched by the Bing Xu group, primarily employing phosphorylated precursors to form cytotoxic fibers upon dephosphorylation by alkaline phosphatases (ALP), overexpressed in cancer cells.⁴² Similarly, MMP-responsive precursors can also transform into nanofibers upon MMP action. The examples in this section and in Table 5 showcase how MMP-triggered formation of nanofibers can selectively kill cancer cells through mechanical damage when used without a drug payload and enhance the efficacy of drug payloads when used in combination.

Tanaka *et al.* designed MMP-7-cleavable lipopeptides, which form nanofibers with high self-assembly propensity upon hydrolysis (Fig. 5A).²⁷ The amphiphilic lipopeptides form spherical micelles and when incubated with MMP-7, the lipid end of the cleaved product self-assembles into fibers within 1 h. These fibers caused selective toxicity to cells *in vitro* that correlated increased toxicity with increased concentration of MMP-7 produced by the cancer cells and was non-toxic to cells with low concentrations of MMP-7. For example, cancerous HeLa cells expressed an MMP-7 concentration that was 6-fold higher than non-cancerous human dermal microvascular endothelial (MvE) cells and displayed a cell viability of ~5% when treated with MMP-7-cleavable lipopeptides. In contrast, MvE cells exhibited a cell viability of over 80%. This stark difference in viability indicates that the cytotoxicity of the system relies on MMP-7 hydrolysis of the lipopeptides to enable the self-assembly of the supramolecular gelator into toxic nanofibers.

Our group has also demonstrated that MMP-9-triggered formation of nanofibers has anti-cancer properties *in vitro* and *in vivo*.⁴³ In this system, approximately spherical peptide micelles (~200 nm in size) were co-assembled with DOX and subsequently cleaved by MMP-9 to form cytotoxic nanofibers. This system is generally represented in Figure 1B without the DOX present in the micelle core pre MMP-cleavage and on the nanofibers after MMP-cleavage. Over 96 h, 60% of the peptide micelles were cleaved by MMP-9 and the resulting cleaved peptides formed bundles of nanofibers. *In vitro* experiments using MMP-9 expressing cells revealed that the MMP-responsive fibers co-assembled with DOX have superior cytotoxicity compared to free DOX. *In vivo* analysis using murine models showed an inhibition of tumor growth in the responsive co-assembled system compared to free DOX. Remarkably, the peptide alone displayed similar tumor growth inhibition effects as DOX alone. This may be due to the peptide aggregates inhibiting the processes of signaling and growth in the cancer cells.



In another study, Yang *et al.* designed cationic multidomain

Fig. 5 Cartoon representation of (A) the lipopeptide that exhibit morphological switching from spherical micelles to nanofibers upon MMP-7 hydrolysis reproduced from reference 27 with permission from Copyright 2015 American Chemical Society and (B) cationic multidomain peptides that change morphology upon MMP-2 incubation from spherical aggregates to nanofibers reproduced from reference 44 with permission from Copyright 2021 Wiley-VCH GmbH.

peptides (MDPs) that demonstrated a structural change upon MMP-2 exposure. The resulting self-assembly formed nanofibers with high membrane activity (Fig. 5B).⁴⁴ MMP-2-responsive MDPs (CS-MDP) contained the cleavable linker, (PLG↓LAG), whereas the non-MMP-2-responsive MDPs

contained a non-cleavable sequence, (LALGPG (NS-MDP)). When treated with MMP-2, CS-MDPs exhibited a structural change from a random coil to β -sheet fiber conformation, whereas NS-MDPs maintained a random coil structure. Moreover, upon extended MMP-2 incubation, CS-MDPs formed nanofibers while NS-MDPs remained as spherical aggregates. Additionally, upon incubation with Nitrobenzoxadiazole (NBD)-labeled CS-MDPs, the cell lines that overexpressed MMP-2 (KYSE-10 and A549) displayed a higher fluorescent intensity compared to cells with low levels of MMP-2 (HeLa). When tested *in vitro*, free DOX was found to be moderately cytotoxic to the three cell lines; however, DOX-loaded CS-MDPs displayed greater toxicity towards the KYSE-10 and A549 cell lines, compared to the HeLa cells. Specifically, a cell viability of 23%, 20%, and 90% was observed towards A549, KYSE-30, and HeLa cells, respectively. The increased efficacy and toxicity observed with the CS-MDPs is due to the enhanced membrane activity upon MMP-2 cleavage and supramolecular assembly. MMP-induced nanofiber formation with or without a loaded therapeutic may be a viable strategy for halting tumor growth.

2.4. Activation by de-PEGylation

Polyethylene glycol or PEG is a hydrophilic block polymer often used as a coating to reduce non-specific interactions and enhance circulation times of nanoparticles. In particular, PEGylation is frequently used as a “stealth” coating approach to enhance circulation of nanoparticles and reduce detection from the immune system.⁴⁵ In the previous examples, the enzymatic removal of PEG groups resulted in changes of the materials' amphiphilic balance that led to particle aggregation or release of smaller inorganic particles from the protective PEG layer. Unlike the examples discussed in section 2.1, the removal of PEG groups from the nanomaterials does not cause a dramatic change in the size of the nanomaterials. On the contrary, these materials are designed to maintain their shape and size after the removal of PEG or “de-PEGylation” by MMP. This strategy allows the nanomaterials to maintain their drug payload within the pre-designed core while revealing or activating the functional targeting ligands that were shielded by the PEG layer. The examples presented in this section and Table 6, utilize the de-PEGylation strategy to slowly release the drug payload from the de-PEGylated and activated nanoparticle instead of a burst release that can accompany a morphology change.

Yao *et al.* have developed MMP-responsive polymer-lipid conjugate building blocks using PEG and phosphoethanolamine (PE) conjugated by the MMP-cleavable linker (GPLG \downarrow IAGQ) and/or a trans-activating transcriptional activator (TAT) peptide that can form paclitaxel-loaded micelles (Fig. 6A).⁴⁶ Two types of paclitaxel-loaded MMP-responsive micelles were synthesized. The first micelle was produced with an exterior coat of PEG (PEG-GPLG \downarrow IAGQ-TAT-PE) and the second with an additional layer of PEG around the lipid core of the micelle (PEG-GPLG \downarrow IAGQ-TAT-PEG-PE). When incubated with bacteria-produced collagenase IV, the micelles without the PEG layer around the core lipid aggregated from \sim 51 nm to \sim 998 nm, whereas the micelles that incorporated PEG surrounding the

core lipid only slightly increased in size from \sim 93 nm to \sim 102 nm. The aggregated micelles showed significant increase in paclitaxel release (80% with and 50% without collagenase, respectively) whereas the non-aggregating micelles did not show a significant increase in drug release (about 50% release with and without collagenase). For the micelles without an interior PEG layer, only (\downarrow IAGQ-TAT-PE) remains post-hydrolysis, which disrupts the amphiphilic balance and the structural integrity of the micelle, resulting in increased release of paclitaxel and aggregation of the post-enzymatic product. Conversely, for the other micelle, the enzymatic cleavage exposes the cell-penetrating TAT peptide on the surface while maintaining the structural integrity of the micelle, (\downarrow IAGQ-TAT-PEG-PE), due to the additional PEG layer in the remaining building block. The TAT-activated and paclitaxel-loaded micelles were able to penetrate the cells and reduce the size of NCI/ADR-RES (ovarian tumor) spheroids significantly compared to the aggregating counter-micelle and were retained longer in murine tumor models *in vivo*.

Ke *et al.* developed a block-co-polymer with poly-D, L lactide and PEG linked by a MMP-2 cleavable linker (PEG-GPLG \downarrow VRGDG-PDLLA) (Fig. 6B).⁴⁷ This construct was demonstrated to encapsulate paclitaxel and form \sim 62 nm spherical micelles. When the particles were incubated with MMP-2, 80% of PEG was cleaved in 25 h, as observed by HPLC. Although the PEG layer was removed, the relative size of the particle remained unchanged. In addition, the MMP-2 cleavage of PEG did not trigger release of paclitaxel. At 72 h, 80% of paclitaxel was released from the micelle with and without incubation with MMP-2. When the PEG is cleaved from this

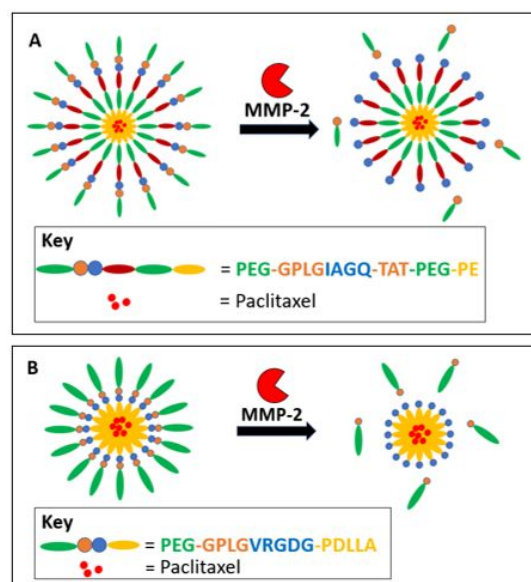


Fig. 6 Cartoon representation (A) MMP-2-responsive multifunctional polymeric micelles reproduced from reference 46 with permission from Copyright 2017 American Chemical Society and (B) MMP-2-responsive amphiphilic block copolymer micelles reproduced from reference 47 with permission from Copyright 2017 American Chemical Society.

micelle, the PDLLA core remains conjugated to (\downarrow VRGDG), which

REVIEW

Biomaterials Science

is sufficiently hydrophilic to keep the particles from aggregating. As a result of this process, the drug remains within the core of the micelle and is unaffected by the MMP-2-triggered cleavage of PEG. The paclitaxel-loaded MMP-activated polymer micelle was more cytotoxic to 4T1 cells (breast tumor) *in vitro* and was able to inhibit tumor growth significantly in H22 (hepatic carcinoma) tumor-bearing mice compared to free paclitaxel *in vivo*.

Table 3. Particle shrinking as a mode of response for anti-cancer therapy.

Pre-MMP cleavage	Post-MMP cleavage	Payload	Targeted MMP	Anti-cancer effects	Ref.
229.4 ± 12.86 nm PEG-coated iron oxide particles	59 ± 3.25 nm Iron oxide particles	Doxorubicin	Non-specific	Increased drug release and cellular uptake, and decreased cancer cell viability <i>in vitro</i>	37
~200 nm Hyaluronic acid-coated dendrimer	~10nm Dendrimer	Doxorubicin	MMP-2	Decreased IC ₅₀ value and enhanced drug uptake <i>in vitro</i> , increased nanoparticle penetration <i>in vitro</i> and <i>in vivo</i> , and increased tumor inhibition rate <i>in vivo</i>	48
193.1 nm Gelatin and dendritic polylysine (DGL) nanoparticles	34.4 nm DGL and gelatin fragments	Doxorubicin	MMP-2	Increased penetration <i>in vitro</i> and <i>in vivo</i> , enhanced nanoparticle retention and tumor growth inhibition, and decreased toxicity of DOX <i>in vivo</i>	49
97.9 ± 2.1 nm Quantum dots (QDs) on gelatin surface	9.7 ± 0.3 nm QDs and gelatin fragments	QD particles	MMP-2	Enhanced diffusive transport <i>in vitro</i> and increased circulation and penetration <i>in vivo</i>	36
117.8 nm Gold and gelatin nanoparticles	< 50.0 nm Gold nanoparticle and gelatin fragments	Doxorubicin	MMP-2	Increased penetration and distribution <i>in vivo</i> and <i>ex vivo</i> and improved tumor growth inhibition ability <i>in vivo</i>	50
185.7 nm Gelatin and DGL nanoparticles	55.6 nm DGL and gelatin fragments	Doxorubicin	MMP-2	Increased cellular uptake of nanoparticles <i>in vitro</i> , enhanced penetration <i>in vitro</i> and <i>in vivo</i> , and significantly higher tumor growth inhibition rate <i>in vivo</i>	51
186.5 ± 2.9 nm Gelatin and gold nanoparticles	59.3 nm Gold nanoparticle and gelatin fragments	Doxorubicin	MMP-2	Enhanced accumulation and penetration efficacy <i>in vitro</i> and <i>in vivo</i> and decreased tumor growth rate <i>in vivo</i>	52
~ 11 nm Gold nanoparticles	~ 2 nm Gold nanoclusters	Gold nanoclusters	MMP-9	Significant increase in colorimetric signal <i>in vivo</i> and no evidence of toxicity <i>in vitro</i> and <i>in vivo</i>	53
188.2 nm Gold and gelatin nanoparticles	55.9 nm Gold nanoparticle and gelatin fragments	Doxorubicin and Cy 5.5	MMP-2	Increased cellular uptake of nanoparticles and improved permeability and penetration <i>in vitro</i> , and better targeting and accumulation efficiency <i>in vivo</i>	54
100.1 ± 13.6 nm PEG-coated mesoporous silica nanoparticles	41.9 ± 3.4 nm Mesoporous silica nanoparticles	Doxorubicin	MMP-2	Improved penetration efficacy <i>in vitro</i> and <i>in vivo</i> and increased tumor growth inhibition and survival rate <i>in vivo</i>	38
85-160 nm Spherical micelles	Irregular shape observed, not quantified	siRNA and Paclitaxel	MMP-2/9	Increased cellular uptake of nanoparticles and RNAi efficiency <i>in vitro</i> and enhanced ability to inhibit tumor growth and metastasis <i>in vitro</i> and <i>in vivo</i>	55
214 ± 5.0 nm Gelatin and platinum nanoparticles	73.9 nm Platinum nanoparticles and gelatin fragments	Telmisartan and Paclitaxel	MMP-2	Increased cellular uptake of nanoparticles and penetration <i>in vitro</i> and enhanced ability to inhibit tumor growth and remodel TME <i>in vivo</i>	56
138 nm Dendritic mesoporous silica nanoparticle linked to ferritin nanocage	85 nm Ferritin nanocage	iTGFβ, oxygen carrying Hb, and ZnPc (photosynthesizer)	MMP-2	Increased permeability and decreased cancer cell viability <i>in vitro</i> and enhanced efficacy in inhibiting primary tumor growth and controlling cancer metastasis <i>in vivo</i>	57

Table 4. Aggregation as a mode of response for anti-cancer therapy.

Pre-MMP cleavage	Post-MMP cleavage	Payload	Targeted MMP	Anti-cancer effects	Ref.
78.2 ± 5.8 nm Spherical micelles	~ 1000 nm Aggregates	siRNA	MMP-2	Enhanced cellular uptake and increased circulation and accumulation <i>in vitro</i> and <i>in vivo</i> , and significant inhibition of tumor growth <i>in vivo</i>	58
20 nm Spherical micelles	Aggregates observed, not quantified.	Paclitaxel	MMP-12	Enhanced tumor growth suppression ability and significantly lower cytotoxicity <i>in vivo</i>	39
86 ± 18 nm Spherical liposomes	109 ± 20 nm Non-specific aggregates	Gemcitabine	MMP-9	Increased drug release efficiency <i>in vitro</i> and reduction in tumor growth rate <i>in vivo</i>	34
33.0 ± 1.2 nm Spherical micelles	818.3 ± 104.7 nm Aggregates	Paclitaxel	MMP-2	Increased drug efficacy, P-glycoprotein (P-gp) inhibition capability, plasma membrane fluidity, inhibition of P-gp ATPase activity, and high drug loading <i>in vitro</i>	59
30 nm Spherical gold nanoparticles	580-630 nm Aggregates	None	MMP-9	Significant reduction in cancer cell viability and increased cellular uptake <i>in vitro</i>	41
73.2 ± 18.8 nm Spherical gold nanoparticles	1.8 × 10 ⁶ ± 1.4 × 10 ⁵ nm Aggregates	Doxorubicin	MMP-2	Enhanced heat production, increased drug release, and strong/broad NIR absorption <i>in vitro</i> , and increased tumor growth inhibition ability, tumor uptake of nanoparticles, and average tumor PA intensity <i>in vivo</i>	40
172 ± 30 nm Spherical polymersomes	>1000 nm Aggregates	SN38	MMP-2	Significant increase in drug release <i>in vitro</i> and improved tumor inhibition efficiency <i>in vivo</i>	60

Table 5. Formation of cytotoxic nanofibers as a mode of response for anti-cancer therapy.

Pre-MMP cleavage	Post-MMP cleavage	Payload	Targeted MMP	Anti-cancer effects	Ref.
Spherical micelles not quantified	Nanofibers not quantified	None	MMP-7	Substantial increase in cytotoxicity to various cancer cell lines and low cytotoxicity to normal cells <i>in vitro</i>	27
200 nm Spherical micelles	Nanofibers not quantified	Doxorubicin	MMP-9	Controlled drug release <i>in vitro</i> and <i>in vivo</i> and increased tumor growth inhibition ability <i>in vivo</i>	43
43.6 ± 6.2 nm Spherical micelles	20-50 nm Nanofibers	Doxorubicin	MMP-9	Controlled release and encapsulation of drug <i>in vitro</i>	61
Spherical aggregates not quantified	268 nm Nanofibers	Doxorubicin	MMP-2	Increased fluorescent intensity and enhanced cellular uptake and drug delivery efficacy <i>in vitro</i>	44
~ 255 nm Spherical nanoparticle	7.3 nm Nanofibers	None	MMP-2	Enhanced efficacy in inhibiting tumor growth and metastasis <i>in vitro</i> and <i>in vivo</i>	62

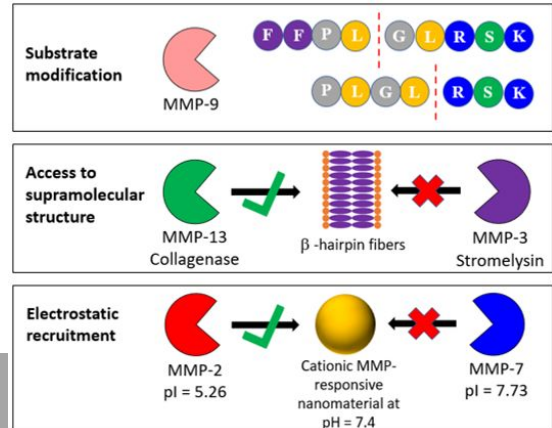
Table 6. De-PEGylation as a mode of response for anti-cancer therapy.

Pre-MMP cleavage	Post-MMP cleavage	Payload	Targeted MMP	Anti-cancer effects	Ref.
62.6 ± 5.1 nm PEGylated micelles	65.2 ± 8.8 nm De-PEGylated micelles	Paclitaxel	MMP-2	Increased cellular uptake of nanoparticles and enhanced cytotoxicity to cancer cells <i>in vitro</i> , and prolonged blood circulation, increased accumulation, and enhanced tumor growth suppression ability <i>in vivo</i>	47
93.4 ± 0.4 nm PEGylated micelles	102.4 ± 6.2 nm De-PEGylated micelles	Paclitaxel	MMP-2	Improved cellular uptake of nanoparticles and tumor penetration, decreased IC ₅₀ value <i>in vitro</i> , and increased tumor uptake of nanoparticles and retention <i>in vivo</i>	46
186.17 ± 5.56 nm PEGylated micelles	215.45 ± 7.85 nm De-PEGylated micelles	Dasatinib	MMP-2	Increased cellular uptake and penetration, significantly decreased IC ₅₀ value <i>in vitro</i> , and prolonged circulation, decreased distribution in non-tumor tissues, and increased tumor accumulation <i>in vivo</i>	63
~ 93 nm PEGylated liposomes	~ 100 nm De-PEGylated liposomes	Sorafenib and Doxorubicin	MMP-2	Increased cellular uptake and decreased IC ₅₀ value <i>in vitro</i> , and inhibited tumor growth and cancer cell proliferation <i>in vitro</i> and <i>in vivo</i>	64
116.1 ± 8.8 nm PEGylated liposomes	153.6 ± 21.7 nm De-PEGylated liposomes	Fluorescein and Paclitaxel prodrug	MMP-9	Reduced cytotoxic effect of prodrug compared to paclitaxel and significantly decreased cancer cell viability <i>in vitro</i>	65
122.1 nm PEGylated nanodots	De-PEGylated nanodots not quantified	Gemcitabine	MMP-2	Enhanced cellular uptake and selective drug release <i>in vitro</i> and enhanced tumor inhibition ability <i>in vivo</i>	66

3. Design guidelines for future advancement of MMP-responsive nanomaterials

In the first half of the review, we analyzed the results of several studies that take advantage of MMP-responsive nanomaterials and their different modes of action *in vitro* and *in vivo* to enhance the selectivity and/or potency (or trigger, in the case of cytotoxic β -sheet fibers) of the active drug and imaging molecules. In the second half of the review, we take another survey of the literature to extract information about which features of the MMP-responsive nanomaterials are most crucial in designing a system that is specific to the targeted MMP and produce the desired mode of action. We have identified 3 key factors that can enhance the interactions between the nanomaterial and enzyme to increase specificity towards the targeted MMP as illustrated in Fig. 7. First and foremost, the primary sequence of the cleavable peptide substrate must meet the consensus for enzyme recognition (single or multiple enzymes), and subtle changes in the amino acids or terminal modification of the primary sequence can alter the cleavage site. However, MMP-cleavable peptide substrates alone display poor specificity due to similar substrate pockets among MMPs, and the possibility of being cleaved by multiple other proteases present in biological samples. Nanomaterials allow incorporation of additional factors to obtain greater control and tunability in achieving desired substrate specificity towards specific MMPs and increase proteolytic stability in samples like human plasma.⁶⁷ Thus, the second factor examines the morphology of nanostructures which can be arranged in such a manner that permits the MMPs to access the cleavable substrate, optimally mimicking the supramolecular context of the natural biological substrates of the target MMP. Lastly, the short-range electrostatic interactions between the nanoparticle and the enzyme can be tuned to optimize responsiveness. For example, based on the isoelectric points (pI) in Figure 9, many secreted MMPs are negatively charged whereas most membrane associated MMPs are positively charged at physiological pH. Thus, the nanomaterials can be designed to have either matching or mis-matching electrostatic interactions in these conditions and can also take advantage of the different pH levels in the tumor vs healthy microenvironment. The responsive nanomaterials we reviewed are made up of various building blocks, such as peptides, lipids, polymers, naturally derived molecules, and inorganic materials that have varying chemical and physical properties (Tables 7-11). Tables 7-11 lists these nanomaterials classified by their chemical composition, and includes their reported morphology, size (or elastic modulus for hydrogels), charge, the MMP-responsive system, the result of the MMP hydrolysis, the targeted MMP, and their applications.

Fig. 7 (1) Modification of the primary sequence can shift the



3.1. Substrate modification

The key component of MMP-responsive nanomaterials is a peptide sequence that can be recognized and hydrolyzed by MMPs in order to induce a physical or chemical change in the nanomaterial. This peptide sequence may be used as a linker to covalently conjugate building blocks together or may confer a structural part of the material itself - in the case of self-assembled peptides. The MMP-cleavable sequence is typically at least 6 amino acids long in order to be recognized by the binding site of the enzyme and is often modified on the C- and N-terminus for attachment to the underlying building blocks of the overall construct.

The amino acid residues in the MMP-cleavable substrate are labeled by the number of positions starting from the scissile bond (cleavage site between P1 and P1') and are labeled P1 through P6 towards the N-terminus, and P1' through P6' towards the C-terminus. Understanding substrate specificity of this family of enzymes can elucidate the functions of specific MMPs,⁶⁸ and help to design more specific inhibitors.⁶⁹ According to the MEROPS database, over 7,600 MMP-cleavable substrates have been observed and recorded.⁷⁰ In addition to natural substrates, many engineered sequences have been identified using various high throughput techniques including phage display,⁷¹ oriented peptide library method,⁷² high capacity (polyethylene glycol-polyacrylamide copolymer (PEGA) supports,⁷³ and proteomic identification of protease cleavage site (PICS).⁷⁴ While MMPs are highly specific enzymes, the general consensus sequence found in the database are similar among MMPs, with Pro in P3, Gly in P1, and Leu in P1' being the hallmark of MMP substrates. As seen in Tables 7-11, a common MMP-cleavable segment frequently used by researchers is PLG↓LAG. We note possible bias towards working with this sequence due to repetition of what has already been explored in the literature.

A thorough examination by Eckhard *et al.* revealed that of 112 cleavages (P1-P1') reported for MMP-1, -2, -3, -7, -8, -9, -12, -13, and -14 in the MEROPS database, only 79 observed cleavage sites were unique, and only 5 sequences contained both Pro in P3 and Leu in P1'.⁷⁴ The authors investigated the substrate specificity of MMPs using fluorescence resonance energy transfer (FRET)-based peptides and peptide hydrolysis was analyzed over time (Figure 7B). In comparison to the general consensus PLG↓L peptide, PLN↓L was cleaved 2.5 times faster by MMP-1 and PAG↓L was cleaved 2 times faster by MMP-2 and 0.25 times faster by MMP-3. Clearly, beyond the general consensus sequence, the primary sequence can be tailored to target specific MMPs.

The sensitivity of the primary sequence can also be observed in cases where a slight change in the order of the amino acids can completely eliminate the activity of the enzyme on that sequence and can be used as negative controls in experiments. For example, GPKG↓LRGD is readily cleaved by MMP-9 whereas GPKL↓GRGD is non-responsive⁴¹ and PLG↓LAG is cleaved by MMP-2 but its scrambled sequence, LAL↓GPG, is non-responsive.⁵⁸

MMP-responsive nanomaterials require the enzyme to interact with the insoluble nanomaterial. The MMP-cleavable substrates are typically covalently modified on the C- and N-terminus of the peptides to act as linkers for block-co-polymers or are used to attach functional moieties – such as targeting ligands – on the surface of the nanomaterial. This modification of the peptide can have significant impact on the enzyme recognition and hydrolysis of the cleavage site. The Bing Xu group has observed that covalent N-terminus modifications with hydrophobic residues of peptides can shift the cleavage site and alter the rate of MMP-9 hydrolysis.⁷⁵ In this study, two sequences were systematically modified by adding one or two phenylalanine residues on the N-terminus followed by capping the terminus with either an acetyl, fluorenylmethyloxycarbonyl (Fmoc), pyrene, or naphthalene group. The researchers observed a shifted cleavage MMP-9 cleavage site with the addition of one or two Phe residues, both with and without the capping groups. Additionally, the rate of hydrolysis decreased with increasing hydrophobicity of the capping group (100% for uncapped, 60% for naphthalene capped, and 30% for Fmoc capped over 72 h). Even a small modification of length and N-terminal substitution can lead to different products and conversion rates. Therefore, more than the primary sequence of the substrate needs to be considered when designing MMP-responsive materials.

3.2. Access to supramolecular structure

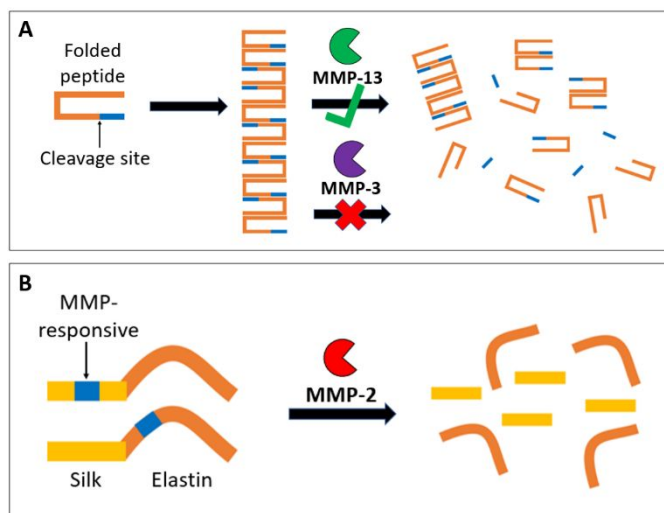
In order for MMPs to cleave the substrate, the enzyme must first interact with the insoluble nanomaterial and have access to the substrate to permit binding. Based on a simplified estimate of spherical proteins with similar molecular weight of MMPs, a 100 nm nanoparticle is about 30-50 times larger than the enzyme (radius of proteins with 10-100 kDa can be calculated to be 2.4- 3.05 nm).⁷⁶ Thus, the diffusion and interaction of the enzyme with the nanomaterial is different from its interaction with a soluble monomeric peptide substrate. Therefore, both the primary sequence of the cleavable substrate and the supramolecular structure of the nanomaterial must be designed to be compatible with the targeted MMP.

The family of MMPs can degrade components of the extracellular matrix ranging from highly ordered proteins such as helical collagen fibers to smaller proteins such as fibronectin or gelatin (Table 1). For instance, MMP-2 and -9 have been reported to bind to native type I collagen but cannot cleave the substrate until it is in the denatured gelatin form, whereas MMP-1 can readily digest the collagen fiber.⁷⁷ Therefore, it would be beneficial to design a less structured (disordered) nanomaterial when targeting MMP-2 or -9, since these gelatinases prefer substrates that possess flexible and unstructured regions, such as those found in denatured collagen, whereas a highly structured (ordered) nanomaterial should be designed when targeting MMP-1, -8, or -13 which prefers more structured substrates like fibrillar collagen. Thus, in addition to the primary sequence, the topology and supramolecular structure of the substrate must also be

appropriate for effective biocatalytic activation by a target MMP.

Several works involving the Pochan and Schneider groups have focused on designing peptides that, upon intramolecular folding of the peptide, self-assemble into β -hairpin hydrogels.⁷⁸⁻⁸⁰ This type of structural specificity was demonstrated by Giano *et al.* using MMP-13-responsive β -hairpin peptide hydrogels (Fig. 8A).⁸¹ These peptides contain two proline residues, one residue between repeating IKV units induces a bend, yielding a β -hairpin structure and the second proline is used to provide the MMP-cleavable substrate PTG \downarrow X, where X = L, I, F, or A. Based on the sequence, both MMPs should be able to cleave PTG \downarrow X, however, the densely packed β -hairpin peptide fibers in the hydrogel were only degraded by MMP-13 that naturally digests collagen fibers and not by MMP-3 which digests sheet-like structures such as the collagen IV, perlecan, *etc.* in the basement membrane (Table 1). In addition, the rate of conversion for MMP-13 degradation of the hydrogel was also dependent on the structural topology of the nanostructures within the gel. According to the sequence specificity, the expected rate of PTG \downarrow X hydrolysis should have followed X = Leu > Ile, Phe > Ala. However, the observed order of degradation was X = Phe (65%) > Leu (58%) > Ile (44%) > Ala (32%), due to the low rigidity and larger pores of the Phe-containing hydrogel, which allows rapid penetration of the gel. This study shows that peptide morphology can be designed to target specific MMPs and the degree of crosslinks in the fiber network can be manipulated to control the rate of hydrogel degradation.

A study by Price *et al.* demonstrated that the location of the MMP-cleavable substrate within the nanostructure can also control the rate of degradation (Fig. 8B).⁸² In this study, silk elastin polymers were modified with a MMP-2 cleavable substrate (GPQGIFGQ) embedded in three locations: 1) between the silk and elastin blocks, 2) within the elastin block, or 3) within the silk block. Higher ratio of digested vs. undigested released polymer was observed when the MMP-cleavable substrate was placed between the silk and the elastin blocks, followed by the substrate embedded within the elastin block, and the substrate imbedded within the silk block had the lowest ratio of digested polymer. This is due to the silk block being a major structural component, and the substrate is more accessible in the block junctions and in the elastin block.



Similarly, in our previous work, we demonstrated that the morphology and the accessibility of the substrate in peptide

Fig. 8 (A) MMP-13-responsive β -hairpin peptide hydrogels reproduced from reference 81 with permission from Copyright 2011 Elsevier and (B) MMP-2-responsive silk-elastin polymer hydrogels reproduced from reference 82 with permission from Copyright 2015 Elsevier.

nanostructures which do not form a gel network can also be manipulated to control the rate of MMP hydrolysis.⁸³ Twelve amphiphilic peptides with a diphenylalanine-containing hydrophobic terminus and either a lysine- or aspartic acid-containing hydrophilic terminus were systematically modified using MMP-9 cleavable PXG \downarrow LXG or AXG \downarrow LXG motif in the center. We observed that among cationic PXG \downarrow LXG containing peptides, spherical micelles were cleaved faster or at the same rate as worm-like micelles. In AXG \downarrow LXG containing cationic peptides, the higher rigidity of the peptide backbone contributed to formation of anti-parallel β -sheet which slowed down the enzyme cleavage kinetics, and MMP-9 was unable to digest these higher ordered fibers.

A study by the Azevedo group showed the importance of supramolecular organization and its effect on the degradation rate of peptide amphiphile (PA) nanofibers.⁸⁴ A series of peptide nanofibers (PS, PA1, PA2, PA3, PA4) were designed with modifications in the alkyl tails as well as the sequence and location of the structural domains. PS displayed a random coil conformation, PA1, PA3, and PA4 nanofibers exhibited a noticeable β -sheet secondary structure, and PA2 nanofibers possessed a combination of secondary structures. After 24 h incubation with MMP-1, ~95% of PS monomers were degraded, compared to limited degradation for PA1 monomers. These results demonstrate the effect of a hydrophobic alkyl tail at the N-terminus of the substrate. Additionally, the effect of supramolecular architecture on degradation efficiency by MMP-1 was explored. PAs that assembled to β -sheet nanofibers demonstrated substantial resistance to MMP-1 degradation. The examples discussed in this section demonstrate how the (dis)order of hydrogels as well as the supramolecular morphology of peptide nanostructures can

decrease or increase MMP-responsiveness by modulating enzyme access to the cleavable substrate.

3.3. Electrostatic recruitment

Electrostatic matching of nanoparticles by decorating them with charged ligands is a commonly used strategy in nanomaterial design and has a significant impact on the kinetics observed in MMP-responsive systems. The substrate binding pockets of MMPs are suited for hydrophobic interactions and typically, the main focus of MMP specificity has been on aromatic and aliphatic residues of the intended substrate. However, as emphasized in this review, the short-range interaction of the MMP and the nanomaterial is also critical to the design. The electrostatic charge of the nanomaterials can be readily tuned to either enhance, or block enzyme engagement and can also be used to target specific MMPs.

In addition, the slightly acidic tumor microenvironment can induce a charge switch that should be considered when designing enzyme responsive materials as targeted therapeutics.⁸⁵ Several MMPs that switch from net negative in healthy environment (pH 7.3 - 7.4) to net positive charge in the tumor microenvironment (< pH 7.2) include MMP-1, 11, 15, 19 (Fig. 9).

The theoretical isoelectric points (pI) of pro-MMPs were computed by Jaiswal *et al.* using ExPASy's ProtParam tool and range broadly from 5.26 to 9.94 (Table 1).²⁸ It is important to note that the pI of MMPs can differ by isoform and charge variants. Using 2D isoelectric focusing, Rossano *et al.* measured and reported pI of 4.1 - 4.6 for several charge variants of 92 kDa pro-MMP-9 and 82 kDa activated MMP-9, and six different charge variants of 65 kDa MMP-9 with pI ranging from 4.82-5.15.⁸⁶ Therefore, in order to find the theoretical pI of active-MMPs used in experiments, we obtained the residues of the catalytic domain (*i.e.* Phe¹⁰⁷-Pro⁴⁴⁹ for MMP-9 from Enzo Biochem) that is commercially available. Using UniProt, we located the residues of the catalytic domain from the full peptide sequence of the human MMP.⁸⁷ Lastly, the theoretical pI of the catalytic domain of the MMP was calculated by plugging the catalytic domain of the full peptide sequence into the ExPASy ProtParam tool and reported as the active pI in Table 1.⁸⁸ Generally, membrane-type MMPs are more basic, with pI values ranging from 5.96 to 9.70, compared to the secreted MMPs which range from 5.26 to 7.73 (except MMP-12 which has pI of 8.75). Using this information, the nanomaterials were designed to have the same or opposite charge to either repel or recruit specific MMPs, respectively. This analysis revealed effective control of the rate of enzyme hydrolysis.

In our aforementioned work, the 12 different MMP-9-responsive self-assembling peptides were systematically modified to have either a positive or negative charge using lysine or aspartic acid residues at the C-terminus, respectively. As expected, the cationic peptides were readily cleaved by MMP-9 (net negative charge at physiological pH) whereas the analogous anionic peptide had very low conversion or were not cleaved at all. This was observed for both spherical and worm-like micelle peptide nanostructures. The electrostatic (mis)-

matching of charges between the nanomaterial and MMP is a simple yet powerful technique to enhance or prevent enzyme cleavage.

We recently reported on two of the aforementioned MMP-9 responsive self-assembling peptides for use as delivery vehicles for hydrophobic payloads.⁸⁹ Two anionic decapeptide sequences were used due to the inability of cationic peptides to encapsulate gold-based therapeutic payloads. The drug-loaded peptides followed similar trends to the unloaded peptides where the disordered Pro containing sequence was cleaved faster than the ordered Ala containing sequence, though with slightly lower hydrolysis kinetics. Surprisingly, both loaded peptides showed similar activity *in vitro*, suggesting the electrostatic recruitment of MMP-9 may be overwhelmed by general proteolytic activity in the vicinity of cancerous cells.

In addition to altering the rate of MMP cleavage, electrostatic specificity can be utilized to target a specific MMP. Yi *et al.* designed a FRET-like system using gold nanorod particles coated with an MMP-cleavable substrate conjugated to a positively charged near-infrared (NIR) dye.⁹⁰ To test the enzyme selectivity of the system, the system was incubated with different MMPs, and their near-infrared fluorescence

(NIRF) signals were measured. The system demonstrated a 6-6-, 8.2-, and 6.6-fold increase in recovery of its NIRF signal against MMP-3, -9, and -13, respectively. However, in the presence of MMP-7, the NIRF signal didn't recover significantly (only 3.7-fold increase) demonstrating the specificity of the system towards certain MMPs. The authors recognized this selectivity but did not comment on likely causes. We speculate that the electrostatic interaction of the modified cationic gold nanorods and the MMPs were favorable for anionic MMP-2, -3 -9, and -13, whereas the near neutral MMP-7 is unlikely to be recruited by the cationic gold nanorods. Using (mis)-matching electrostatic interactions between the enzyme and the nanostructures, the enzyme cleavage rate and specificity can be controlled.

Keeping the three design guidelines in mind, nanomaterials can be designed to take advantage of the innate properties and activity of MMPs in cancer progression and optimized using substrate specificity, suitable supramolecular structure, and (mis)-matching electrostatics of the targeted MMP to deliver the anti-cancer response with maximum selectivity.

Charge of MMPs (pro form) at different pH levels															
Type	MMP	Tumor microenvironment													Healthy environment
		pH = 5.6	pH = 5.7	pH = 5.8	pH = 5.9	pH = 6	pH = 6.1	pH = 6.2-6.3	pH = 6.4	pH = 6.5	pH = 6.6-6.9	pH = 7	pH = 7.1	pH = 7.2	
Secreted	7	+	+	+	+	+	+	+	+	+	+	+	+	+	+
	26	+	+	+	+	0	-	-	-	-	-	-	-	-	-
	1	+	+	+	+	+	+	+	+	0	-	-	-	-	-
	3	+	+	0	-	-	-	-	-	-	-	-	-	-	-
	8	+	+	+	+	+	+	+	0	-	-	-	-	-	-
	10	-	-	-	-	-	-	-	-	-	-	-	-	-	-
	12	+	+	+	+	+	+	+	+	+	+	+	+	+	+
	13	-	-	-	-	-	-	-	-	-	-	-	-	-	-
	19	+	+	+	+	+	+	+	+	+	+	+	+	0	-
	20	+	+	+	+	+	+	+	+	+	+	+	+	+	+
	27	+	+	+	+	+	+	+	+	+	+	+	+	+	+
	2	-	-	-	-	-	-	-	-	-	-	-	-	-	-
	9	+	0	-	-	-	-	-	-	-	-	-	-	-	-
	11	+	+	+	+	+	+	+	0	-	-	-	-	-	-
	28	+	+	+	+	+	+	+	+	+	+	+	+	+	+
21	+	+	+	+	+	+	+	+	+	+	+	+	+	+	
14	+	+	+	+	+	+	+	+	+	+	+	+	+	+	
Membrane associated	15	+	+	+	+	+	+	+	+	+	+	0	-	-	
	16	+	+	+	+	+	+	+	+	+	+	+	+	+	
	24	+	+	+	+	+	+	+	+	+	+	+	+	+	
	17	+	+	+	+	+	0	-	-	-	-	-	-	-	
	25	+	+	+	+	+	+	+	+	+	+	+	+	+	
	23	+	+	+	+	+	+	+	+	+	+	+	+	+	

Fig. 9 Charge of the 23 human MMPs (pro form) at pH levels ranging from 5.6-7.2 (tumor microenvironment) and 7.3-7.4 (healthy microenvironment). A positive charge (blue) is indicated by a plus sign, a negative charge (red) is indicated by a negative sign, and a neutral charge (green) is indicated by a zero.

Table 7. Peptide-based MMP-responsive nanomaterials and hydrogels.

Chemical composition	Morphology	Diameter Size(nm) / Hydrogel Modulus (Pa)	Charge (mV)	MMP-responsive system	MMP hydrolysis	Targeted MMP	Application	Ref.			
Self-assembled peptide	Anti-parallel β - sheet fiber	300	11.5 \pm 0.8	FFALG \downarrow LAGKK	0% conversion at 96 h (1 mM peptide + 100 ng/mL MMP-9)	MMP-9	Design	83			
		250	-34.9 \pm 1.1	FFALG \downarrow LAGDD	0% conversion at 96 h (1 mM peptide + 100 ng/mL MMP-9)						
	Worm-like micelle	250	15.4 \pm 0.3	FFPLG \downarrow LAGKK	100% conversion at 72 h (1 mM peptide + 100 ng/mL MMP-9)						
		10	-38.0 \pm 1.7	FFPLG \downarrow LAGDD	~ 8% conversion at 96 h (1 mM peptide + 100 ng/mL MMP-9)						
		5	8.2 \pm 2.8	FFGALG \downarrow LK GK	~ 60% conversion at 96 h (1 mM peptide + 100 ng/mL MMP-9)						
		10	-30.3 \pm 1.4	FFGALG \downarrow LDGD	~ 7% conversion at 96 h (1 mM peptide + 100 ng/mL MMP-9)						
		30	1.3 \pm 0.6	FFGAAG \downarrow LK GK	~ 5% conversion at 96 h (1 mM peptide + 100 ng/mL MMP-9)						
		10	-7.5 \pm 1.8	FFGAAG \downarrow LDGD	0% conversion at 96 h (1 mM peptide + 100 ng/mL MMP-9)						
	Spherical micelle	50	4.1 \pm 1.0	FFGPLG \downarrow LK GK	100% conversion at 48 h (1 mM peptide + 100 ng/mL MMP-9)						
		500	-41.2 \pm 2.3	FFGPLG \downarrow LDGD	100% conversion at 96 h (1 mM peptide + 100 ng/mL MMP-9)						
		100	1.1 \pm 1.5	FFGPAG \downarrow LK GK	~ 80% conversion at 96 h (1 mM peptide + 100 ng/mL MMP-9)						
		100	-28.2 \pm 0.7	FFGPAG \downarrow LDGD	~ 80% conversion at 96 h (1 mM peptide + 100 ng/mL MMP-9)						
	Spherical micelle	43.6 \pm 6.2	N/A	Phenylacetyl-FFAGL \downarrow DD	100% conversion at 96 h (5 mM peptide + 50 ng/mL MMP-9)				MMP-9	Proof of concept drug delivery	61
	Spherical micelle	200	N/A	GFFLGL \downarrow DD	~ 60% conversion at 96 h (2.5 mM peptide + 50 ng/mL MMP-9)				MMP-9	Drug delivery (<i>in vitro</i> and <i>in vivo</i>)	43
Polyproline α - helical filament	~ 10 (filaments)	N/A	N/A	Acetyl-KKY-GPQG \downarrow IAGQ-YKK-NH ₂	Observed degradation at 6 h	MMP-2	Design	91			
		N/A	N/A	Acetyl-KKY-IPVS \downarrow LRSG-YKK-NH ₂	Observed degradation at 6 h						

Table 7 (Contd.)

Chemical composition	Morphology	Diameter Size(nm) / Hydrogel Modulus (Pa)	Charge (mV)	MMP-responsive system	MMP hydrolysis	Targeted MMP	Application	Ref.
Self-assembled peptide hydrogel	β - hair pin	820 (G')	N/A	IKVKIKVKV(d)-PPTG \downarrow FKVKIKV-NH ₂	~ 65% conversion at 14 days (1 wt.% peptide + 80 nM MMP-13) and 0% conversion at 14 days (40 or 400 nM MMP-3)	MMP-13	Cell migration (<i>in vitro</i>)	81
		1900 (G')	N/A	IKVKIKVKV(d)-PPTG \downarrow LKVKIKV-NH ₂	~ 58% conversion at 14 days (1 wt.% peptide + 80 nM MMP-13)			
		2800 (G')	N/A	IKVKIKVKV(d)-PPTG \downarrow IKVKIKV-NH ₂	~ 44% conversion at 14 days (1 wt.% peptide + 80 nM MMP-13)			
		350 (G')	N/A	IKVKIKVKV(d)-PPTG \downarrow AKVKIKV-NH ₂	~ 32% conversion at 14 days (1 wt.% peptide + 80 nM MMP-13)			
	β - sheet fiber	175 (G')	N/A	K-SLSLSLRG \downarrow SLSLSL-K	100% conversion after 48 h (1 wt.% peptide + 100 ng MMP-2)	MMP-2	Cell migration (<i>in vitro</i>)	92
	β - sheet fiber	~ 1000 (G')	N/A	Acetyl-IIIS \downarrow LKG-NH ₂	~ 60% conversion at 15 days (8 mM peptide + 100 ng/mL MMP-2)	MMP-2	Anti-cancer peptide delivery (<i>in vitro</i>)	93
~ 1000 (G')		N/A	Acetyl-IIIS \downarrow LGK-NH ₂	0% conversion at 15 days (8 mM peptide + 100 ng/mL MMP-2)				
	Hydrogel	~ 140-210 (G')	N/A	FFFFCG \downarrow LDD	52.8% conversion after 2 h (0.6 wt.% peptide + 8 μ U of MMP-9)	MMP-9	Design/ Method development	94

Table 8. Lipid-based MMP-responsive nanomaterials.

Chemical composition	Morphology	Diameter Size (nm) / Hydrogel Modulus (Pa)	Charge (mV)	MMP-responsive system	MMP hydrolysis	Targeted MMP	Application	Ref.
Liposome	Spherical	65.4 ± 2.3	-22.1 ± 0.3	SDK-C ₁₈ -SGPLG↓IAGQSK-C ₁₈ -DS	100% conversion at 3h (100 μM substrate only + 0.2 μg/mL MMP-2) and ~ 90% conversion from smooth to unsmooth particles	MMP-2	Drug delivery (<i>in vitro</i> and <i>in vivo</i>)	95
	Spherical	~ 93	~ -7	DOPE-SA-PEG-Lysine-PE-PLG↓IAG-PEG	~ 70% DOX and 60% SRF release at 72 h	MMP-2	Drug delivery (<i>in vitro</i> and <i>in vivo</i>)	64
	Spherical	207.5 ± 75.5	-10.23 ± 1.21	DOPE-GPLG↓IAGQ--PEG- mAb	100% conversion at 24 h (1 mg/mL polymer + 10 ng/μL MMP-2)	MMP-2	Drug delivery (<i>in vitro</i>)	96
	Spherical	86 ± 18	N/A	POPE-GPQG↓IAGQR-PEG	Size increase and drug release: 24 h (2 μM MMP-9)	MMP-9	Drug delivery (<i>in vitro</i> and <i>in vivo</i>)	34
	Spherical	116.1 ± 8.8	-7.23 ± 15.56	PTX-SRLS↓LPGC- PEG	Fluorescein release at 24h (20 μg MMP-expressing cell supernatant)	MMP-9	Drug delivery (<i>in vitro</i>)	65
Lipid micelle	Spherical	N/A	N/A	C ₁₆ -GGGHGPLG↓LARK-CONH ₂	> 50% conversion within 1 h (0.2 wt.% lipopeptide + 2 μg/mL MMP-7)	MMP-7	Anti-cancer gelator delivery (<i>in vitro</i>)	27
	Non-spherical	61.3 ± 15	N/A	PEG-GPLG↓IAGQ-PTX	100% conversion overnight (2.5 mg/mL micelle solution + 5 ng/μL MMP-2)	MMP-2	Drug delivery (<i>in vitro</i> and <i>in vivo</i>)	30
	Spherical	16.5 ± 5.1	26.8 ± 2.4	PEG-GPLG↓IAGQ-PEI-PE	100% conversion overnight (1 mg/mL polymer + 5 ng/μL MMP2)	MMP-2	Drug delivery (<i>in vitro</i> and <i>in vivo</i>)	97
	Spherical	33.0 ± 1.2	~0	PEG-GPLG↓IAGQ-PE	Size change measured at 2h and drug release increase at 2, 4 and 48 h (50 μg/mL collagenase IV)	MMP-2	Drug delivery (<i>in vitro</i>)	59
	Spherical	93.4 ± 0.4	1.9 ± 0.2	PEG-GPLG↓IAGQ-YGRKKRRQRRRC (TAT)-PEG-PE	~ 70% conversion at 12 h (2 mg/ml polymer + 10 ng/ml MMP-2)	MMP-2	Drug delivery (<i>in vitro</i> and <i>in vivo</i>)	46
	Oval	186.17 ± 5.56	-15.05 ± 1.84	PEG-GPLG↓IAGQ-PE	Size change, zeta potential, and drug release measured at 1 h (50 μg/mL collagenase IV)	MMP-2	Drug delivery (<i>in vitro</i> and <i>in vivo</i>)	63
	Spherical	69.5 ± 10.6	8.2 ± 3.4	PEG-GPLG↓IAGQ-YGRKKRRQRRRC (TAT)-DOX	100% conversion (1 mg/mL PEG-pp-TAT-DOX + 6 ng/μL of MMP-2)	MMP-2	Drug delivery (<i>in vitro</i>)	98

Table 9. Polymer-based MMP-responsive nanomaterials and hydrogels.

Chemical composition	Morphology	Diameter Size (nm) / Hydrogel Modulus (Pa)	Charge (mV)	MMP-responsive system	MMP hydrolysis	Targeted MMP	Application	Ref.
Polymer micelle	Spherical	43.5	N/A	PEG-GPLG↓VRG DG-PBLA	70% conversion after 16 h (5.52 mg/2mL polymer + 1 µg/mL MMP-2)	MMP-2	Drug delivery (<i>in vitro</i>)	31
	Spherical	62.6 ± 5.1	N/A	PEG-GPLG↓VRG DG-PDLLA	> 70% conversion within 8 h (1 µg/mL MMP-2)	MMP-2	Drug delivery (<i>in vitro</i> and <i>in vivo</i>)	47
	Spherical	78.2 ± 5.8	34.7 ± 2.8	PEG-PLG↓LAG (R) ₉ -PCL	100% conversion at 1h (5 mg/mL nanoparticles + 2 µg/mL of MMP-2)	MMP-2	siRNA delivery (<i>in vitro</i> and <i>in vivo</i>)	58
	Spherical	133.3 ± 12	N/A	Pluronic-GPVG↓LIGK-Pluronic-GPVG↓LIGK-Pluronic	100% conversion by 24 h (25 wt.% polymer + 250 µg/mL collagenase IV)	MMP-2	Drug delivery (<i>in vitro</i>)	99
	Spherical	121	-21.8 ± 1.28	PEG-E ₁₀ -PLG↓LAG-VSR ₆ GGR ₄ -PCL	Increased penetration and accumulation <i>in vitro</i> and drug accumulation <i>in vivo</i>	MMP-2/9	Drug delivery (<i>in vitro</i> and <i>in vivo</i>)	100
	Spherical	24	N/A	Copolymer (1 ₃₄ -b-2 ₁₄)-LRRASLGKGPLG↓LAG	Size change observed at 24 h (20 µM micelle solution + 100 µU MMP-2/9)	MMP-2/9	Design	101
	Spherical	33	N/A	Copolymer (1 ₃₄ -b-2 ₁₄)-KKPLG↓LAG LRRASLG	~ 21% conversion at 24 h (20 µM micelle solution + 100 µU MMP-2/9)			
	Spherical	20	N/A	Copolymer-dye (1 ₁₀ -b-2 ₃ -Alexa647)-GPLG↓LAGGWGER DGS	Size change observed at 24 h (1 µM NP + 10 nM MMP-9)	MMP-9	Imaging (<i>in vivo</i> and <i>ex vivo</i>)	102
PAMAM dendrimer	Spherical	5.4	N/A	PAMAM-PLG↓LAG-Cy5	<i>In vivo</i> fluorescence	MMP-2/9	Imaging (<i>in vivo</i>)	103
	Spherical	~200	-32.2	HA-PLG↓LAG-PAMAM	Significant size change observed after 4 h (4 mg/mL nanoparticles + 0.5 mg/mL MMP-2)	MMP-2	Drug delivery (<i>in vitro</i> and <i>in vivo</i>)	48
Nanocapsule	Spherical	20 - 45	1.4	AAM-APM-KLGPAK	Degradation observed, not quantified at 30 min (50 unit/mL collagenase)	Non-specific	Protein delivery (<i>in vitro</i>)	104

Table 9 (Contd.)

Chemical composition	Morphology	Diameter Size(nm) / Hydrogel Modulus (Pa)	Charge (mV)	MMP-responsive system	MMP hydrolysis	Targeted MMP	Application	Ref.
PLA based nanoparticle (NP)	Spherical	112.47 ± 3.21	-21.52 ± 3.16	AKRGARSTAC (LinTT1)-PVG↓LIG-GRKKRRQRRRC (TAT)-NP-PTX	~ 80% of PTX released in plasma at 72 h	MMP-2/9	Drug delivery (<i>in vitro</i> and <i>in vivo</i>)	105
Telechelic block copolymer	Cross-linked hydrogel	N/A	N/A	Acrylate -APG↓L-PEG-APG↓L- Acrylate	~ 100% conversion in 110 h (0.35 g gel + 2 mg/mL collagenase type I)	MMP-1	Design	106
Synthetic MMP substrate	Soluble form	N/A	N/A	Ac-GPQG↓IWGQ-NH ₂	Kcat/Km: 870 ± 170 M ⁻¹ s ⁻¹ (40 nM MMP-1)	MMP-1	Design/ Method development	107
		N/A	N/A	Ac-GCRD-GPQG↓IWGQ-DRCG-NH ₂	Kcat/Km: 1,760 ± 280 M ⁻¹ s ⁻¹ (40 nM MMP-1)			
		N/A	N/A	Ac-GCRD-GPQG↓IAGQ-DRCG-NH ₂	Kcat/Km: 400 ± 80 M ⁻¹ s ⁻¹ (40 nM MMP-1)			
	Hydrogel	N/A	N/A	PEG-Ac-GCRD-GPQG↓IWGQ-DRCG-NH ₂	Kcat/Km: 2,130 ± 430 M ⁻¹ s ⁻¹ (40nM MMP-1)			
		N/A	N/A	PEG-Ac-GCRD-GPQG↓IWGQ-DRCG-NH ₂	Kcat/Km: 970 ± 190 M ⁻¹ s ⁻¹ (40 nM MMP-1)			
PEG based	Hydrogel	N/A	N/A	8-PEG-Ac-FKGGGPQG↓IWGQ-ERCG-NH ₂	100% gel degradation at 9 h (40 nM MMP-1)	MMP-1	Design/ Method development	108
Mesoporous silica NP	Spherical	100.1 ± 13.6	~ 18	MSNs-GPLG↓IAGQ-PEG	Size change observed at 3 h (300 ng/mL MMP-2)	MMP-2	Drug delivery (<i>in vitro</i> and <i>in vivo</i>)	38
Chimeric polymersome	Spherical	172 ± 30	-18.2	PEG-PVG↓LIG-PLA	Significant degradation observed after 24 h and complete drug release at 240 h (10 nM MMP-2)	MMP-2	Drug delivery (<i>in vitro</i> and <i>in vivo</i>)	60

Table 10. Naturally derived-based MMP-responsive nanomaterials and hydrogels.

Chemical composition	Morphology	Diameter Size(nm) / Hydrogel Modulus (Pa)	Charge (mV)	MMP-responsive system	MMP hydrolysis	Targeted MMP	Application	Ref.
Silk elastin protein polymer	Soluble monomer	N/A	N/A	Silk-GPQG↓IFGQ-elastin-lysine elastin-elastin-silk (RS1)	~ 100% conversion at 1 h (1 mg/mL polymer + 40 nM MMP-2)	MMP-2	Gene delivery (<i>in vivo</i>)	82
		N/A	N/A	Silk-elastin GPQG↓IFGQ-lysine elastin-elastin-silk (RS2)	~ 100% conversion at 1h (1 mg/mL polymer + 40 nM MMP-2).			
		N/A	N/A	Silk-GPQG↓IFGQ-silk-elastin-lysine elastin-elastin-silk (RS5)	~ 100% conversion at 1 h (1 mg/mL polymer + 40 nM MMP-2)			
	Hydrogel	N/A	N/A	Silk-GPQG↓IFGQ-elastin-lysine elastin-elastin-silk (RS1)	Up to 185% increase in soluble fraction released at 14 d (4 wt.% and 8 wt.% polymer + 40 nM MMP-2)			
		N/A	N/A	Silk-elastin GPQG↓IFGQ-lysine elastin-elastin-silk (RS2)	Up to 185% increase in soluble fraction released at 14 d (4 wt.% and 8 wt.% polymer + 40 nM MMP-2)			
		N/A	N/A	Silk-GPQG↓IFGQ-silk-elastin-lysine elastin-elastin-silk (RS5)	< 20% increase in soluble fraction released at 14 d (4 wt.% and 8 wt.% polymer + 40 nM MMP-2)			
Alginate	Hydrogel	120 ± 24 (G')	N/A	Alginate (LMW)-GGYGPVG↓LIGGK	Cell migration of culture at 7 d (2 wt.% polymer)	MMP produced by hMSC	Cell implantation (<i>in vivo</i>)	109
Dendrimer-gelatin NP	Spherical	193.1	N/A	RGD-DOX-DGL-Gelatin type A NP	Fluorescent imaging <i>in vitro</i> and <i>in vivo</i>	MMP-2	Drug delivery (<i>in vitro</i> and <i>in vivo</i>)	49
Polypeptide based nanogel	Cross-linked nanogel	14.7	N/A	Gelatin type B-surfactant (CTAB)-succinic anhydride (Suc)	60% of hydrophobic dye released at 24 h (0.65 mg nanogel solution + 2.84 μg MMP-9)	MMP-9	Drug delivery (<i>in vitro</i>)	110
Collagen IV	Triple helical	N/A	N/A	Collagen IV	83% digestion in 15 mins (5 – 100 ng/mL MMP-9)	MMP-9	Method development	111
PAMAM dendrimer in collagen gel	Triple helical	N/A	N/A	Collagen peptide-DOX-dendrimer-embedded collagen type IV	Biological activity <i>in vitro</i> and <i>in vivo</i>	MMP-9	Drug delivery (<i>in vitro</i> and <i>in vivo</i>)	112

Table 11. Inorganic-based MMP-responsive nanomaterials.

Chemical composition	Morphology	Diameter Size (nm) / Hydrogel Modulus (Pa)	Charge (mV)	MMP-responsive system	MMP hydrolysis	Targeted MMP	Application	Ref.
Gold (Au) nanorod	Nanorod	40 (l) x 20 (w)	N/A	Cy5.5-GPLG↓VRGC-Au nanorod	NIRF signal recovery: 7.8x increase at 1 h (6.75 nM MMP-2) 6.6x increase at 2 h (MMP-3) 8.2x increase at 2 h (MMP-9) 6.6x increase at 2 h (MMP-13) 3.7x increase at 2 h (MMP-7)	MMP-2, -3, -7, -9, -13	Phototherapy (<i>in vitro</i> and <i>in vivo</i>)	90
Quantum dot (QD) gelatin NP	Spherical	97.9 ± 2.1	-6.29 ± 0.22	Gelatin type A NPs	~ 90% of QDs released at 12 h (0.1 mg NP + 230 ng MMP-2)	MMP 2	Proof of concept NP delivery	36
PEG hydrogel-coated magnetic iron oxide NP	Spherical and ellipsoid	229.4 ± 12.86	-3.37 ± 0.28	Acrylate-PEG-GGGPQG↓IWGQGK-PEG-acrylate	60% of DOX released after 3 d and at the end of 4 d (0.1 mg/mL collagenase type I)	Non-specific	Drug delivery (<i>in vitro</i>)	37
CdSe/ZnS QD	Near-spherical	12.8 ± 3.6	-8.4	PEG-GGPLGVGRGK-NH ₂	Cleavage and payload release <i>in vivo</i>	MMP-9	Drug delivery (<i>in vitro</i> and <i>in vivo</i>)	113
Gelatin NP (GNP) linked to platinum NP (PtNP)	Spherical	214 ± 5.0	-12.3 ± 7.2	Gelatin type B NPs(Telmisartan)-PEG-PtNPs-SeSe-PTX	~ 65% decrease in particle size after 8 h	MMP-2	Drug delivery (<i>in vitro</i> and <i>in vivo</i>)	56
Aggregation-induced emission nanodot	Spherical	122.1	-1.27	α-CD-TPR-GEM-PEG-R ₈ -PLG↓LAG-(EK) ₆	~ 100% of GEM released at 96 h	MMP-2	Drug delivery (<i>in vitro</i> and <i>in vivo</i>)	66
Gold Nanocluster (AuNC)-Neutravidin (NAv) complex	AuNC-NAv complex	~ 11	N/A	AuNC-Biotin-GGGPLG↓VRGKGGC-NAv AuNC-Biotin-GGGGGGGGGPLG↓VRGKGGC-NAv	~ 20% of AuNCs liberated at 1 h 100% degradation within 4.5 h (50 nM MMP-9) and ~ 80% of AuNCs liberated at 1 h	MMP-9	Diagnostic sensor (<i>in vitro</i> and <i>in vivo</i>)	53

4. Future Perspectives

Significant progress has been made in the field of MMP-responsive nanomaterials, however, many challenges remain to be addressed before these materials can be successfully translated into clinical use. The upregulation of MMP activity not only varies in different cancers, but in different stages and grades of the same cancer. As outlined in this review, MMP-responsive nanomaterials are highly dependent upon the overexpression and activity of the MMP to trigger desired changes within the nanomaterial. Since cancer progression changes over time and different tissues present different mechanical and chemical properties, tailoring of contextual, spatial, and temporal aspects is essential. Additionally, MMPs display promiscuous activity within the family, cleaving similar peptides with varying rates due to shared substrate pockets. Multiple optimized consensus sequences for specific MMPs further complicate peptide substrate selection, as untargeted MMPs may cleave them more rapidly than the targeted MMPs. In addition, endogenous inhibitors and interactions in the cellular microenvironment can decrease MMP activity, allowing the possibility that untargeted MMPs and other proteases can cleave the peptide substrates as well. Understanding these complexities is crucial when designing biomaterials based on MMP-specific peptides, as specificity for a targeted MMP does not ensure specific cleavage by that protease alone. In addition to this complexity, determining and comparing the anti-cancer efficacy of different systems proved to be challenging due to the various methods of data measurement employed for the reported *in vitro* and *in vivo* studies. There is a wide range of useful data that can be collected for both *in vitro* and *in vivo* experiments which demonstrate the anti-cancer performance of a system. These experiments include measuring cell internalization, the IC₅₀ value, drug release rate, and cytotoxicity for *in vitro* data; and tumor weight and volume, animal body weight, survival time, and tumor growth inhibition rate for *in vivo* data. Hence, due to the inconsistencies in the method of data collection and reporting across the different systems, resolving whether one system had a more effective anti-cancer effect between different papers was not feasible. For example, the tumor growth inhibition rate is calculated as a percentage and is dependent upon the mean tumor weight of treated and control groups, whereas tumor volume, measured in mm³, considers the width and length rather than mass. Although both types of data can be used to portray the anti-cancer efficacy of a system, we cannot directly compare the tumor growth inhibition rate to the tumor volume to assess the system's anti-tumor effectiveness based on the data reported in literature. Moreover, even in cases where authors have similar types of data, factors such as the subtype of cancer and the cell lines used vary. These inconsistencies make it challenging to compare systems across different papers.

This raises questions of not only which data is necessary in determining and proving the anti-cancer effectiveness of a system, but also what classifies a system as effective. Broadly, the effectiveness of a system is defined by the system's ability to shrink tumor size and kill cells. However, as observed in this

review, MMP-responsive systems are not always demonstrated to increase the toxicity, nor tumor-reducing ability of the payloads. Instead, some systems achieve more selective and targeted therapy, potentially reducing adverse side effects that would transform current chemotherapy into safer treatment options. Additionally, even if proven successful in pre-clinical studies, many of these MMP-responsive systems fail, potentially because they are being evaluated at the wrong endpoints in clinical trials.

In addition to comparing the anti-cancer efficacy in *in vitro* and *in vivo* studies, we also found it difficult to compare the MMP-responsiveness from one system to another based on the data reported. For example, some papers report on the enzyme responsiveness based on the rate of payload release or the cleavage of an isolated peptide substrate. However, as observed in Section 2.4, the release of payload is not triggered by MMP-cleavage when using the de-PEGylation strategy but rather on the hydrolysis of the post-cleavage nanomaterial. Likewise, the rate of cleavage measured on a soluble peptide is different from the rate of cleavage when the peptide is embedded in a nanostructure (Section 3.2). Therefore, these results cannot be quantitatively compared and cannot be used to draw more subtle deductions on details such as whether a spherical⁴⁶ or oval⁶³ shaped lipid micelle is more responsive to MMP-2. Nonetheless, we included the rate of MMP-responsiveness that was reported in literature in Tables 7-11 as helpful suggestions when designing new systems. Using the three key design guidelines discussed in this review and building on the decades of extensive research, there is great potential for MMP-responsive nanomaterials to advance towards translational research with greater specificity and enhanced functionality, both which are essential for successful targeted anti-cancer therapy.

5. Concluding remarks

In this review, we analyzed a variety of MMP-responsive systems and have outlined key design guidelines to achieve both specificity and functionality in MMP-responsive nanomaterials. The main factors taken into consideration include substrate modification, supramolecular architecture and electrostatic charge of the nanomaterial. Moreover, we evaluated how the different modes of nanomaterial response can control and amplify the spatial and temporal effects of the anti-cancer treatments *in vitro* and *in vivo*, such as controlled rate of the payload release. Specifically, size-shrinking particles can induce greater tumor penetration and cell internalization; induced aggregation can decrease the overall systematic toxicity *in vivo* and increase potency in drug-resistant cells; formation of cytotoxic nanofibers can achieve highly selective mechanical toxicity *in vitro* and enhance the efficacy of drugs *in vivo* when used in combination; and de-PEGylation can expose targeting ligands without significantly changing the morphology or size of the nanoparticle, allowing the payloads to remain within the core and release slowly. These comprehensive strategies endow MMP-responsive nanomaterials with promising potential as effective anti-cancer treatments.

Author Contributions

J.S. and S.P. contributed equally to the completion of this manuscript. J.S. accepted the theme of the literature review and analysis; S.P. created original figures and tables and organized the manuscript; J.S., S.P., D.M, Y.M, and R.H.H analyzed previous works in literature and wrote original summaries; and R.V.U provided critical feedback and revisions to the manuscript, focusing on improving the clarity, organization, and messages of this manuscript.

Conflicts of interest

There are no conflicts to declare.

Acknowledgements

We thank PSC-CUNY PROGRAM YEAR 52 Award (J.S. and S.P.); Tow Foundation Graduate Fellowship from the MSKCC Center for Molecular Imaging and Nanotechnology (J.S.); CUNY Summer Undergraduate Research Program and the Alfred P. Sloan Foundation (S.P.); National Science Foundation Grant CHE 1808143 (R.V.U. and R.H.H.); Office of Naval Research Vannevar Bush Faculty Fellowship Grant N00014-21-1-2967 (R.V.U.). This work is partially supported by the National Science Foundation CREST Center for Interface Design and Engineered Assembly of Low Dimensional systems (IDEALS), NSF Grant HRD-1547830.

References

- P. S Burrage, K. Mix and C. Brinckerhoff, *Matrix metalloproteinases: Role in arthritis*, 2006, vol. 11.
- H. Kai, H. Ikeda, H. Yasukawa, M. Kai, Y. Seki, F. Kuwahara, T. Ueno, K. Sugi and T. Imaizumi, *Journal of the American College of Cardiology*, 1998, **32**, 368–372.
- Z. S. Galis, G. K. Sukhova, M. W. Lark and P. Libby, *J Clin Invest*, 1994, **94**, 2493–2503.
- M. G. Tutton, M. L. George, S. A. Eccles, S. Burton, R. I. Swift and A. M. Abulafi, *International Journal of Cancer*, 2003, **107**, 541–550.
- T. A. Giamberrardi, G. M. Grant, G. P. Taylor, R. J. Hay, V. M. Maher, J. J. McCormick and R. J. Klebe, *Matrix Biol.*, 1998, **16**, 483–496.
- M. W. Roomi, J. C. Monterrey, T. Kalinovsky, M. Rath and A. Niedzwiecki, *Oncol. Rep.*, 2009, **21**, 1323–1333.
- E. M. Yousef, M. R. Tahir, Y. St-Pierre and L. A. Gaboury, *BMC Cancer*, 2014, **14**, 609.
- G. Bergers, R. Brekken, G. McMahon, T. H. Vu, T. Itoh, K. Tamaki, K. Tanzawa, P. Thorpe, S. Itohara, Z. Werb and D. Hanahan, *Nature Cell Biology*, 2000, **2**, 737–744.
- C. Gialeli, A. D. Theocharis and N. K. Karamanos, *FEBS Journal*, 2011, **278**, 16–27.
- J. E. Meisel and M. Chang, *Biochimica et Biophysica Acta (BBA) - Molecular Cell Research*, 2017, **1864**, 2001–2014.
- G. B. Fields, *Front. Immunol.*, 2019, **10**, 1278.
- M. Hidalgo and S. G. Eckhardt, *JNCI Journal of the National Cancer Institute*, 2001, **93**, 178–193.
- M. Egeblad and Z. Werb, *Nat. Rev. Cancer*, 2002, **2**, 161–174.
- P. Sarkar, Z. Li, W. Ren, S. Wang, S. Shao, J. Sun, X. Ren, N. G. Perkins, Z. Guo, C.-E. A. Chang, J. Song and M. Xue, *J. Med. Chem.*, 2020, **63**, 6979–6990.
- J. Cathcart, A. Pulkoski-Gross and J. Cao, *Genes & Diseases*, 2015, **2**, 26–34.
- A. Winer, S. Adams and P. Mignatti, *Mol Cancer Ther.*, DOI:10.1158/1535-7163.MCT-17-0646.
- P. D. Brown, *APMIS*, 1999, **107**, 174–180.
- R. E. Vandenbroucke and C. Libert, *Nat Rev Drug Discov*, 2014, **13**, 904–927.
- L. M. Coussens, B. Fingleton and L. M. Matrisian, *Science*, 2002, **295**, 2387–2392.
- G. B. Fields, *Cells*, 2019, **8**, 984.
- H. Nagase and J. F. Woessner, *J. Biol. Chem.*, 1999, **274**, 21491–21494.
- H. Nagase, R. Visse and G. Murphy, *Cardiovascular Research*, 2006, **69**, 562–573.
- S. Loffek, O. Schilling and C.-W. Franzke, *European Respiratory Journal*, 2011, **38**, 191–208.
- H.-J. Ra and W. C. Parks, *Matrix Biology*, 2007, **26**, 587–596.
- A. Anadón, V. Castellano and M. R. Martínez-Larrañaga, in *Biomarkers in Toxicology*, Elsevier, 2014, pp. 923–945.
- D. Hanahan and R. A. Weinberg, *Cell*, 2000, **100**, 57–70.
- A. Tanaka, Y. Fukuoka, Y. Morimoto, T. Honjo, D. Koda, M. Goto and T. Maruyama, *J. Am. Chem. Soc.*, 2015, **137**, 770–775.
- A. Jaiswal, A. Chhabra, U. Malhotra, S. Kohli and V. Rani, *Bioinformation*, 2011, **6**, 23–30.
- T. Iizasa, T. Fujisawa, M. Suzuki, S. Motohashi, K. Yasufuku, T. Yasukawa, M. Baba and M. Shiba, *Clin Cancer Res*, 1999, **5**, 149–153.
- L. Zhu, T. Wang, F. Perche, A. Taigind and V. P. Torchilin, *PNAS*, 2013, **110**, 17047–17052.
- W. Ke, J. Li, K. Zhao, Z. Zha, Y. Han, Y. Wang, W. Yin, P. Zhang and Z. Ge, *Biomacromolecules*, 2016, **17**, 3268–3276.
- Z.-H. Peng and J. Kopeček, *Journal of the American Chemical Society*, 2015, **137**, 6726–6729.
- Y. Chau, R. F. Padera, N. M. Dang and R. Langer, *Int. J. Cancer*, 2006, **118**, 1519–1526.
- P. S. Kulkarni, M. K. Haldar, R. R. Nahire, P. Katti, A. H. Ambre, W. W. Muhonen, J. B. Shabb, S. K. R. Padi, R. K. Singh, P. P. Borowicz, D. K. Shrivastava, K. S. Katti, K. Reindl, B. Guo and S. Mallik, *Mol. Pharmaceutics*, 2014, **11**, 2390–2399.
- A. I. Minchinton and I. F. Tannock, *Nature Reviews Cancer*, 2006, **6**, 583–592.
- C. Wong, T. Stylianopoulos, J. Cui, J. Martin, V. P. Chauhan, W. Jiang, Z. Popović, R. K. Jain, M. G. Bawendi and D. Fukumura, *PNAS*, 2011, **108**, 2426–2431.
- C. Nazli, G. S. Demirer, Y. Yar, H. Y. Acar and S. Kizilel, *Colloids and Surfaces B: Biointerfaces*, 2014, **122**, 674–683.
- X. He, D. Wang, P. Chen, Y. Qiao, T. Yang, Z. Yu, C. Wang and H. Wu, *Chem. Commun.*, 2020, **56**, 4785–4788.
- C. E. Callmann, C. V. Barback, M. P. Thompson, D. J. Hall, R. F. Mattrey and N. C. Gianneschi, *Adv. Mater.*, 2015, **27**, 4611–4615.
- K. Yang, Y. Liu, Y. Wang, Q. Ren, H. Guo, J. B. Matson, X. Chen and Z. Nie, *Biomaterials*, 2019, **223**, 119460.
- R. H. Huang, N. Nayeem, Y. He, J. Morales, D. Graham, R. Klajn, M. Contel, S. O'Brien and R. V. Ulijn, *Advanced Materials*, 2021, adma.202104962.
- J. Zhou and B. Xu, *Bioconjugate Chemistry*, 2015, **26**, 987–999.
- D. Kalafatovic, M. Nobis, J. Son, K. I. Anderson and R. V. Ulijn, *Biomaterials*, 2016, **98**, 192–202.

- 44 S. Yang, Y. Chang, S. Hazoor, C. Brautigam, F. W. Foss, Z. Pan and H. Dong, *ChemBioChem*, 2021, cbic.202100323.
- 45 J. S. Suk, Q. Xu, N. Kim, J. Hanes and L. M. Ensign, *Advanced Drug Delivery Reviews*, 2016, **99**, 28–51.
- 46 Q. Yao, Z. Dai, J. Hoon Choi, D. Kim and L. Zhu, *ACS Appl. Mater. Interfaces*, 2017, **9**, 32520–32533.
- 47 W. Ke, Z. Zha, J. F. Mukerabigwi, W. Chen, Y. Wang, C. He and Z. Ge, *Bioconjugate Chem.*, 2017, **28**, 2190–2198.
- 48 M. Han, M.-Y. Huang-Fu, W.-W. Guo, N.-N. Guo, J. Chen, H.-N. Liu, Z.-Q. Xie, M.-T. Lin, Q.-C. Wei and J.-Q. Gao, *ACS Appl. Mater. Interfaces*, 2017, **9**, 42459–42470.
- 49 G. Hu, H. Zhang, L. Zhang, S. Ruan, Q. He and H. Gao, *International Journal of Pharmaceutics*, 2015, **496**, 1057–1068.
- 50 X. Cun, S. Ruan, J. Chen, L. Zhang, J. Li, Q. He and H. Gao, *Acta Biomaterialia*, 2016, **31**, 186–196.
- 51 G. Hu, X. Chun, Y. Wang, Q. He and H. Gao, *Oncotarget*, 2015, **6**, 41258–41274.
- 52 S. Ruan, X. Cao, X. Cun, G. Hu, Y. Zhou, Y. Zhang, L. Lu, Q. He and H. Gao, *Biomaterials*, 2015, **60**, 100–110.
- 53 C. N. Loynachan, A. P. Soleimany, J. S. Dudani, Y. Lin, A. Najer, A. Bekdemir, Q. Chen, S. N. Bhatia and M. M. Stevens, *Nat. Nanotechnol.*, 2019, **14**, 883–890.
- 54 S. Ruan, Q. He and H. Gao, *Nanoscale*, 2015, **7**, 9487–9496.
- 55 S. Tang, Q. Meng, H. Sun, J. Su, Q. Yin, Z. Zhang, H. Yu, L. Chen, Y. Chen, W. Gu and Y. Li, *Adv. Funct. Mater.*, 2016, **26**, 6033–6046.
- 56 T. Fang, J. Zhang, T. Zuo, G. Wu, Y. Xu, Y. Yang, J. Yang and Q. Shen, *ACS Appl. Mater. Interfaces*, 2020, **12**, 31292–31308.
- 57 T. Liang, B. Zhang, Z. Xing, Y. Dong, H. Xu, X. Chen, L. Jiang, J. Zhu and Q. Min, *Angew. Chem. Int. Ed.*, 2021, **60**, 11464–11473.
- 58 H.-X. Wang, X.-Z. Yang, C.-Y. Sun, C.-Q. Mao, Y.-H. Zhu and J. Wang, *Biomaterials*, 2014, **35**, 7622–7634.
- 59 Z. Dai, Q. Yao and L. Zhu, *ACS Appl. Mater. Interfaces*, 2016, **8**, 12661–12673.
- 60 P. Ramezani, K. Abnous, S. M. Taghdisi, M. Zahiri, M. Ramezani and M. Aliboland, *Colloids and Surfaces B: Biointerfaces*, 2020, **193**, 111135.
- 61 D. Kalafatovic, M. Nobis, N. Javid, P. W. J. M. Frederix, K. I. Anderson, B. R. Saunders and R. V. Ulijn, *Biomater. Sci.*, 2015, **3**, 246–249.
- 62 W. Zhang, J. Hu, R. Liu, J. Dai, L. Yuan, Y. Liu, B. Chen, M. Gong, F. Xia and X. Lou, *Advanced Science*, 2023, 2207228.
- 63 Q. Yao, J. H. Choi, Z. Dai, J. Wang, D. Kim, X. Tang and L. Zhu, *ACS Appl. Mater. Interfaces*, 2017, **9**, 36642–36654.
- 64 L. Kou, R. Sun, X. Jiang, X. Lin, H. Huang, S. Bao, Y. Zhang, C. Li, R. Chen and Q. Yao, *ACS Appl. Mater. Interfaces*, 2020, **12**, 30031–30043.
- 65 D. Ehrsam, S. Sieber, M. Oufir, F. Porta, M. Hamburger, J. Huwyler and H. E. Meyer zu Schwabedissen, *Bioconjugate Chem.*, 2020, **31**, 781–793.
- 66 X. Chen, H. Gao, Y. Deng, Q. Jin, J. Ji and D. Ding, *ACS Nano*, 2020, **14**, 5121–5134.
- 67 Y. Marciano, N. Nayeem, D. Dave, R. V. Ulijn and M. Contel, *ACS Biomater. Sci. Eng.*, 2023, **9**, 3379–3389.
- 68 B. I. Ratnikov, P. Cieplak, K. Gramatikoff, J. Pierce, A. Eroshkin, Y. Igarashi, M. Kazanov, Q. Sun, A. Godzik, A. Osterman, B. Stec, A. Strongin and J. W. Smith, *PNAS*, 2014, **111**, E4148–E4155.
- 69 M. Mikhailova, X. Xu, T. K. Robichaud, S. Pal, G. B. Fields and B. Steffensen, *Matrix Biol*, 2012, **31**, 380–388.
- 70 N. D. Rawlings, A. J. Barrett, P. D. Thomas, X. Huang, A. Bateman and R. D. Finn, *Nucleic Acids Res*, 2018, **46**, D624–D632.
- 71 S. J. Kridel, E. Chen, L. P. Kotra, E. W. Howard, S. Mobashery and J. W. Smith, *J. Biol. Chem.*, 2001, **276**, 20572–20578.
- 72 B. E. Turk, L. L. Huang, E. T. Piro and L. C. Cantley, *Nat. Biotechnol.*, 2001, **19**, 661–667.
- 73 M. Renil, M. Ferreras, J. M. Delaisse, N. T. Foged and M. Meldal, *J Pept Sci*, 1998, **4**, 195–210.
- 74 U. Eckhard, P. F. Huesgen, O. Schilling, C. L. Bellac, G. S. Butler, J. H. Cox, A. Dufour, V. Goebeler, R. Kappelhoff, U. A. dem Keller, T. Klein, P. F. Lange, G. Marino, C. J. Morrison, A. Prudova, D. Rodriguez, A. E. Starr, Y. Wang and C. M. Overall, *Matrix Biol.*, 2016, **49**, 37–60.
- 75 Y. Huang, J. Shi, D. Yuan, N. Zhou and B. Xu, *Biopolymers*, 2013, **100**, 790–795.
- 76 H. P. Erickson, *Biol Proced Online*, 2009, **11**, 32–51.
- 77 I. E. Collier, W. Legant, B. Marmer, O. Lubman, S. Saffarian, T. Wakatsuki, E. Elson and G. I. Goldberg, *PLoS One*, , DOI:10.1371/journal.pone.0024029.
- 78 T. Yucl, C. M. Micklitsch, J. P. Schneider and D. J. Pochan, *Macromolecules*, 2008, **41**, 5763–5772.
- 79 M. C. Branco, F. Nettesheim, D. J. Pochan, J. P. Schneider and N. J. Wagner, *Biomacromolecules*, 2009, **10**, 1374–1380.
- 80 C. Veerman, K. Rajagopal, C. S. Palla, D. J. Pochan, J. P. Schneider and E. M. Furst, *Macromolecules*, 2006, **39**, 6608–6614.
- 81 M. C. Giano, D. J. Pochan and J. P. Schneider, *Biomaterials*, 2011, **32**, 6471–6477.
- 82 R. Price, A. Poursaid, J. Cappello and H. Ghandehari, *J Control Release*, 2015, **213**, 96–102.
- 83 J. Son, D. Kalafatovic, M. Kumar, B. Yoo, M. A. Cornejo, M. Contel and R. V. Ulijn, *ACS Nano*, , DOI:10.1021/acsnano.8b07401.
- 84 Y. Shi, D. S. Ferreira, J. Banerjee, A. R. Pickford and H. S. Azevedo, *Biomater. Sci.*, 2019, **7**, 5132–5142.
- 85 L. Wang, M. Huo, Y. Chen and J. Shi, *Adv. Healthcare Mater.*, 2018, **7**, 1701156.
- 86 R. Rossano, M. Larocca, L. Riviello, M. G. Coniglio, J. Vandooren, G. M. Liuzzi, G. Opdenakker and P. Riccio, *J. Cell. Mol. Med.*, 2014, **18**, 242–252.
- 87 UniProt, <https://www.uniprot.org/>, (accessed August 13, 2022).
- 88 ExPASy - ProtParam tool, <https://web.expasy.org/protparam/>, (accessed August 13, 2022).
- 89 Y. Marciano, V. del Solar, N. Nayeem, D. Dave, J. Son, M. Contel and R. V. Ulijn, *J. Am. Chem. Soc.*, 2023, **145**, 234–246.
- 90 D. K. Yi, I.-C. Sun, J. H. Ryu, H. Koo, C. W. Park, I.-C. Youn, K. Choi, I. C. Kwon, K. Kim and C.-H. Ahn, *Bioconjugate Chem.*, 2010, **21**, 2173–2177.
- 91 Y.-A. Lin, Y.-C. Ou, A. G. Cheetham and H. Cui, *Biomacromolecules*, 2014, **15**, 1419–1427.
- 92 K. M. Galler, L. Aulisa, K. R. Regan, R. N. D'Souza and J. D. Hartgerink, *J. Am. Chem. Soc.*, 2010, **132**, 3217–3223.
- 93 C. Chen, Y. Zhang, Z. Hou, X. Cui, Y. Zhao and H. Xu, *Biomacromolecules*, 2017, **18**, 3563–3571.
- 94 Z. Yang, M. Ma and B. Xu, *Soft Matter*, 2009, 10.1039.b908206a.
- 95 T. Ji, J. Lang, J. Wang, R. Cai, Y. Zhang, F. Qi, L. Zhang, X. Zhao, W. Wu, J. Hao, Z. Qin, Y. Zhao and G. Nie, *ACS Nano*, 2017, **11**, 8668–8678.
- 96 L. Zhu, P. Kate and V. P. Torchilin, *ACS Nano*, 2012, **6**, 3491–3498.
- 97 L. Zhu, F. Perche, T. Wang and V. P. Torchilin, *Biomaterials*, 2014, **35**, 4213–4222.
- 98 Y. Tu and L. Zhu, *Journal of Controlled Release*, 2015, **212**, 94–102.
- 99 V. K. Garripelli, J.-K. Kim, S. Son, W. J. Kim, M. A. Repka and S. Jo, *Acta Biomaterialia*, 2011, **7**, 1984–1992.

- 100G. Gu, H. Xia, Q. Hu, Z. Liu, M. Jiang, T. Kang, D. Miao, Y. Tu, Z. Pang, Q. Song, L. Yao, H. Chen, X. Gao and J. Chen, *Biomaterials*, 2013, **34**, 196–208.
- 101T.-H. Ku, M.-P. Chien, M. P. Thompson, R. S. Sinkovits, N. H. Olson, T. S. Baker and N. C. Gianneschi, *J. Am. Chem. Soc.*, 2011, **133**, 8392–8395.
- 102M.-P. Chien, A. S. Carlini, D. Hu, C. V. Barback, A. M. Rush, D. J. Hall, G. Orr and N. C. Gianneschi, *J. Am. Chem. Soc.*, 2013, **135**, 18710–18713.
- 103E. S. Olson, T. Jiang, T. A. Aguilera, Q. T. Nguyen, L. G. Ellies, M. Scadeng and R. Y. Tsien, *Proc. Natl. Acad. Sci. U.S.A.*, 2010, **107**, 4311–4316.
- 104J. Wen, S. M. Anderson, J. Du, M. Yan, J. Wang, M. Shen, Y. Lu and T. Segura, *Adv. Mater.*, 2011, **23**, 4549–4553.
- 105Z. Sun, R. Li, J. Sun, Y. Peng, L. Xiao, X. Zhang, Y. Xu and M. Wang, *ACS Appl. Mater. Interfaces*, 2017, **9**, 40614–40627.
- 106J. L. West and J. A. Hubbell, *Macromolecules*, 1999, **32**, 241–244.
- 107M. P. Lutolf, J. L. Lauer-Fields, H. G. Schmoekel, A. T. Metters, F. E. Weber, G. B. Fields and J. A. Hubbell, *Proceedings of the National Academy of Sciences*, 2003, **100**, 5413–5418.
- 108M. Ehrbar, S. C. Rizzi, R. G. Schoenmakers, B. San Miguel, J. A. Hubbell, F. E. Weber and M. P. Lutolf, *Biomacromolecules*, 2007, **8**, 3000–3007.
- 109K. B. Fonseca, D. B. Gomes, K. Lee, S. G. Santos, A. Sousa, E. A. Silva, D. J. Mooney, P. L. Granja and C. C. Barrias, *Biomacromolecules*, 2014, **15**, 380–390.
- 110K. Kim, B. Bae, Y. J. Kang, J.-M. Nam, S. Kang and J.-H. Ryu, *Biomacromolecules*, 2013, **14**, 3515–3522.
- 111A. Shoji, M. Kabeya and M. Sugawara, *Analytical Biochemistry*, 2011, **419**, 53–60.
- 112C. Kojima, T. Suehiro, K. Watanabe, M. Ogawa, A. Fukuhara, E. Nishisaka, A. Harada, K. Kono, T. Inui and Y. Magata, *Acta Biomaterialia*, 2013, **9**, 5673–5680.
- 113H. Han, D. Valdepérez, Q. Jin, B. Yang, Z. Li, Y. Wu, B. Pelaz, W. J. Parak and J. Ji, *ACS Nano*, 2017, **11**, 1281–1291.